

**Monitoring the vegetation vigor in heterogeneous citrus and olive orchards. A multiscale object-based approach to extract trees' crowns from UAV multispectral imagery**

Giuseppe MODICA<sup>1\*</sup>, Gaetano MESSINA<sup>1</sup>, Giandomenico DE LUCA<sup>1</sup>,  
Vincenzo FIOZZO<sup>1</sup>, and Salvatore PRATICÒ<sup>1</sup>

Dipartimento di Agraria, Università degli Studi Mediterranea di Reggio Calabria,  
Località Feo di Vito, I-89122 Reggio Calabria, Italy

\**Corresponding author:* Giuseppe Modica, [giuseppe.modica@unirc.it](mailto:giuseppe.modica@unirc.it)

# 1        **Monitoring the vegetation vigor in heterogeneous citrus and olive** 2        **orchards. A multiscale object-based approach to extract trees' crowns** 3        **from UAV multispectral imagery**

## 4 5        **Abstract**

6        Precision agriculture (PA) constitutes one of the most critical sectors of remote sensing applications that allow  
7        obtaining spatial segmentation and within-field variability information from field crops. In the last decade, an  
8        increasing source of information is provided by unmanned aerial vehicle (UAVs) platforms, mainly equipped with  
9        optical multispectral cameras, to map, monitor, and analyze, temporal and spatial variations of vegetation using  
10        ad hoc spectral vegetation indices (VIs). Considering the centimeter or sub-centimeter spatial resolution of UAV  
11        imagery, the geographic object-based image analysis (GEOBIA) approach, is becoming prevalent in UAV remote  
12        sensing applications. In the present paper, we propose a quick and reliable semi-automatic workflow implemented  
13        to process multispectral UAV imagery and aimed at the detection and extraction of olive and citrus trees' crowns  
14        to obtain vigor maps in the framework of PA. We focused our attention on the choice of GEOBIA data input and  
15        parameters, taking into consideration its replicability and reliability in the case of heterogeneous tree orchards.  
16        The heterogeneity concerns the different tree plantation distances and composition, different crop management  
17        (irrigation, pruning, weeding), and different tree age, height, and crown diameters. The proposed GEOBIA  
18        workflow was implemented in the eCognition Developer 9.5, coupling the use of multispectral and topographic  
19        information surveyed using the Tetracam  $\mu$ -MCA06 snap multispectral camera at 4 cm of ground sample distance  
20        (GSD). Three different study sites in heterogeneous citrus (Bergamot and Clementine) and olive orchards located  
21        in the Calabria region (Italy) were provided. Multiresolution segmentation was implemented using spectral and  
22        topographic band layers and optimized by applying a trial-and-error approach. The classification step was  
23        implemented as process-tree and based on a rule set algorithm, therefore easily adaptable and replicable to other  
24        datasets. Decision variables for image classification were spectral vegetation indices (NDVI, SAVI, CVI) and  
25        topographic layers (DSM and CHM). Vigor maps were based on NDVI and NDRE and allowed to highlight those  
26        areas with low vegetative vigor. The accuracy assessment was based on a per-pixel approach and computed  
27        through the F-score (F). The obtained results are promising, considering that the resulting accuracy was high, with  
28        F-score ranging from 0.85 to 0.91 for olive and bergamot, respectively. Our proposed workflow, which has proved  
29        effective in datasets of different complexity, finds its strong point is the speed of execution and on its repeatability  
30        to other different crops with few adjustments. It appears worth of interest to highlights that it requests a working  
31        day of two good skilled operators in geomatics and computer image processing, from the on-field data collection  
32        to the obtaining of vigor maps.

33  
34        **Keywords:** multispectral unmanned aerial vehicles (UAVs) imagery; multiresolution segmentation; Precision  
35        Agriculture (PA); spectral Vegetation Indices (VIs); geographic object-based image analysis (GEOBIA); vigor  
36        maps.

## 37 **1. Introduction**

38 Bergamot (*Citrus bergamia*, Risso) crops are mainly located on the Ionian sea coast in the province of Reggio  
39 Calabria (South Italy). The fruit was primarily cultivated for the extraction of essential oil from the peel to  
40 use it in the cosmetic, perfumery (Jin et al., 2016) and food industries (Pernice et al., 2009). Since 2001, these  
41 productions awarded the European protected designation of origin (PDO) label *Bergamotto di Reggio*  
42 *Calabria – olio essenziale* (“Bergamot of Reggio Calabria - essential oil”). In the food industry, an increasing  
43 interest has focused on the use of bergamot’s juice as a beverage and in a blend with other fruit juices (Giuffrè,  
44 2019). This interest is related to the antioxidant properties of juice, beneficial for health (Da Pozzo et al.,  
45 2018). From the dried and processed waste is obtained the so-called *pastazzo*, which can be used as animal  
46 feed (Nesci and Sapone, 2014). Over 90% of the world’s bergamot production comes from Calabria while  
47 the remaining 10% from Africa (Côte d’Ivoire, Mali, Cameroon, Guinea) and South America (Argentina and  
48 Brazil) (Nesci and Sapone, 2014). Clementine (*Citrus clementina* Hort. ex Tan.) is one of the essential  
49 cultivated varieties of citrus mandarins in the Mediterranean Basin (Benabdelkamel et al., 2012). Italy is one  
50 of the largest producers in Europe, and its crops are located in the southern part of the country. Productions  
51 made in the Calabria region are labeled with the European protected geographical indication label  
52 “Clementine di Calabria” (Benabdelkamel et al., 2012). Olive (*Olea europaea* L.) crops represent a critical  
53 agricultural production in the Mediterranean Basin, and the Calabria region is one of the primary Italian olive  
54 oil producers. Moreover, olive crops can be considered as a distinctive trait of the historical rural landscape  
55 of the Mediterranean Basin (Di Fazio and Modica, 2018).

56 To achieve an effective, sustainable environmental management of crop productions coupling with an  
57 improvement of agriculture competitiveness of the agriculture sector, precision agriculture (PA)  
58 methodologies and technologies currently represent a reliable and cost-effective approach (Solano et al.,  
59 2019). The International Society for Precision Agriculture (ISPA), defines the PA as “a management strategy  
60 that gathers, processes and analyzes temporal, spatial and individual data and combines it with other  
61 information to support management decisions according to estimated variability for improved resource use  
62 efficiency, productivity, quality, profitability and sustainability of agricultural production  
63 ([www.ispag.org/about/definition](http://www.ispag.org/about/definition), last access 30 April 2020). PA that can be viewed as a management strategy  
64 aiming at implementing agronomic interventions in line with real crop needs and the biochemical and

65 physical characteristics of the soil constitutes one of the most critical sectors of remote sensing applications  
66 (De Montis et al., 2017).

67 As highlighted by several scholars, PA allows to increase crop productivity and farm profitability through  
68 the better management of farm inputs (Larson and Robert, 1991; Zhang et al., 2002) and using intensive data  
69 and information collection. In the framework of PA, remote sensing techniques allow obtaining spatial  
70 segmentation and within-field variability information from field crops (Sepulcre-Cantó et al., 2005).  
71 Traditionally, remote sensing has been associated with satellite platforms or manned aircrafts equipped with  
72 a series of sensors (Pajares, 2015) while, since the last decade, the advent of unmanned aerial vehicles  
73 (UAVs) platforms constitutes one of the primary sources of remote sensing imagery in PA.

74 Moreover, continuous technological improvement concerns UAV platforms as well as the typology of  
75 mounted sensors in terms of radiometric resolution, weight, optical characteristics, etc. (Romero-Trigueros  
76 et al., 2017). Compared to satellite platforms, UAVs have the advantage of providing images with very high  
77 spatial and temporal resolution coupled with an ever-increasing radiometric resolution that is leading to a  
78 production cost efficiency. As highlighted by Benincasa et al. (2017), UAV surveys are more suitable than  
79 satellite remote sensing in cloudy conditions, in case of small surfaces and when a centimeter spatial  
80 resolution is needed.

81 Typically, UAV applications in PA dealing with the following research issues: weed and disease detection  
82 (Abdulridha et al., 2019; Albetis et al., 2018; De Castro et al., 2018; De Castro et al., 2015; Maes and Steppe,  
83 2019; Pérez-Ortiz et al., 2016; Torres-Sánchez et al., 2015), assessment of vegetation coverage and typology  
84 (Ampatzidis and Partel, 2019; Candiago et al., 2015; Senthilnath et al., 2017), analysis, monitoring and  
85 assessment of biomass and vegetation vigor (Bendig et al., 2015; Díaz-Varela et al., 2015; W. Li et al., 2016;  
86 Malambo et al., 2018; Panagiotidis et al., 2017; Roth and Streit, 2018; Zarco-Tejada et al., 2014). The  
87 increasing interest of several scholars focused on the trees' crown extraction from UAV imagery in the  
88 framework of PA applications (Caruso et al., 2019; Díaz-Varela et al., 2015; Koc-San et al., 2018; Ok and  
89 Ozdarici-Ok, 2018; Solano et al., 2019).

90 Currently, UAVs equipped with multispectral cameras represent the most commonly exploited remote  
91 sensing systems in agriculture (Khanal et al., 2017). These systems have the advantage of being able to obtain  
92 spectral information in the red (R) and near-infrared (NIR) regions of the electromagnetic spectrum that allow  
93 deriving vegetation indices (VIs) useful for applications in PA (Yao and Qin, 2019). In the framework of PA,

94 remote sensing applications can provide essential information to map, monitor, and analyze temporal and  
95 spatial variations of vegetation vigor. Although an increasing number of VIs is currently available for PA  
96 applications, most of them are obtained combining information in R and NIR regions of electromagnetic  
97 spectrum. Beyond a high correlation with the biophysical parameters of plants, VIs have a reduced sensitivity  
98 to all those factors that hinder the interpretation of remote sensing data, such as soil background and  
99 atmosphere (Wójtowicz et al., 2016).

100 In the last two decades, remote sensing technologies have been improved in order to be able to use more  
101 effective methods of extracting reliable and reusable information in the framework of PA applications  
102 (Solano et al., 2019). Among these techniques, the geographic object-based image analysis (GEOBIA)  
103 approach, that allows detecting geographical entities through the definition and the analysis of object-images  
104 instead of single pixels (Blaschke, 2010; Hay and Castilla, 2008), is becoming prevalent in UAV remote  
105 sensing (Li et al., 2016). Moreover, the GEOBIA approach allows capturing the rapid change of geographic  
106 objects in very high-resolution UAV imagery, including the shadow effect of trees, typically higher than in  
107 satellite or aerial imagery, due to a larger parallax effect considering the lower distance between the surveyed  
108 objects and the sensor.

109 GEOBIA defines a typology of a digital remote sensing image analysis approach that studies geographical  
110 entities through the definition and analysis of object-based instead of single pixels (Blaschke, 2010; Blaschke  
111 et al., 2014; Hay and Castilla, 2008). Image objects are objects that can be visually distinguished in the image  
112 and made up of groups (or clusters) of neighboring pixels that share a common context or meaning, such as  
113 pixels that join together to form the canopy of a tree or crops in a field (Chen et al., 2018). GEOBIA  
114 demonstrated effectiveness in classifying weeds, herbaceous (De Castro et al., 2018, 2017, Peña et al., 2015,  
115 2013, 2012; Pérez-Ortiz et al., 2016, 2015), and tree species (Csillik et al., 2018; Díaz-Varela et al., 2015;  
116 Koc-San et al., 2018; Ozdarici-Ok, 2015; Solano et al., 2019).

117 Within the scientific and technological framework briefly outlined, the present paper has a twofold research  
118 objective. The first one is devoted to showing a quick and reliable semi-automatic workflow implemented to  
119 process multispectral UAV imagery. The proposed workflow is aimed at the detection and extraction of olive  
120 and citrus trees' crowns in the framework of PA with the final production of vigor maps showing the  
121 vegetative state of the tree crowns. The second one focuses on the choice of GEOBIA data input and  
122 parameters reliable in the case of heterogeneous tree orchards. The heterogeneity concerns the different tree

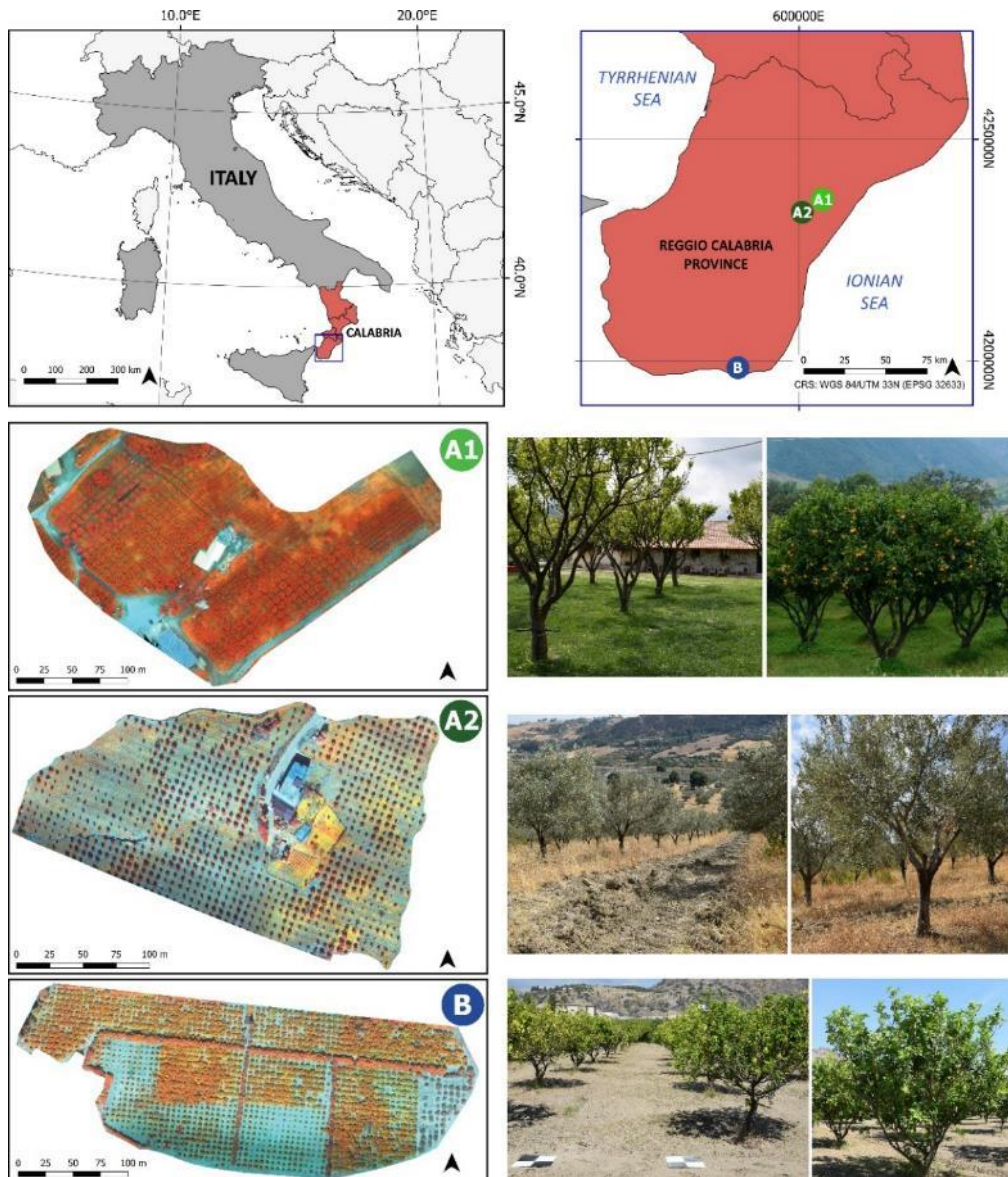
123 plantation distances, the different crop management (irrigation, pruning, weeding, etc.), the different crop  
124 composition, and on the different tree age, height, and crown diameters. The proposed GEOBIA workflow  
125 was implemented in the eCognition Developer 9.5 (Trimble Inc., 2019), coupling the use of multispectral  
126 (radiometric bands and their different combinations/ratios) and topographic information. Three different  
127 study sites in heterogeneous citrus (Bergamot and Clementine) and olive orchards located in the Calabria  
128 region (Italy), were provided.

129 The structure of this paper is as follows. In Section 2, we provided a brief description of the three analyzed  
130 study sites. Section 3 deals with materials and methods, providing details about data acquisition, data  
131 processing workflow, GEOBIA procedures, the analyzed VIs, and about the implemented accuracy  
132 assessment procedure. In Section 4, the results of segmentation, classification, trees extraction processes,  
133 accuracy assessment, and final vigor maps produced, are presented and discussed. Finally, Section 5 deals  
134 with conclusions and future research outlooks.

135

## 136 **2. Study sites**

137 All three-study sites are located in the province of Reggio Calabria (Calabria, Italy) (Fig. 1), A1 and A2 in  
138 Antonimina municipality (38°15'52'' N, 16°11'12'' E, 111 m a.s.l., and 38°16'12'' N, 16°11' 04'' E, 193  
139 m a.s.l., respectively), study site B in the municipality of Palizzi (37° 55' 06'' N, 15° 58' 54'' E, 4 m a.s.l.).  
140 Study A1 is a 15-year even-aged (3.5 m height) citrus orchard (clementine, *Citrus x clementina*) with a 5m  
141 x 5m single-tree planting distance covering an area of 4.6 ha. The study site A2 covers 7.12 ha and is a 20-  
142 year even-aged specialized olive orchard with a 6m x 6m single-tree planting distance. Both orchards are  
143 managed according to organic farming methods. The study site B is an uneven-aged citrus orchard (bergamot,  
144 *Citrus bergamia*) with long windbreak barriers made up of olive trees, and covering an area of 7.9 ha. This  
145 orchard is particularly heterogeneous, being composed of trees with age ranging from 5 years (1.5 m height)  
146 to 25 years (4 m height).

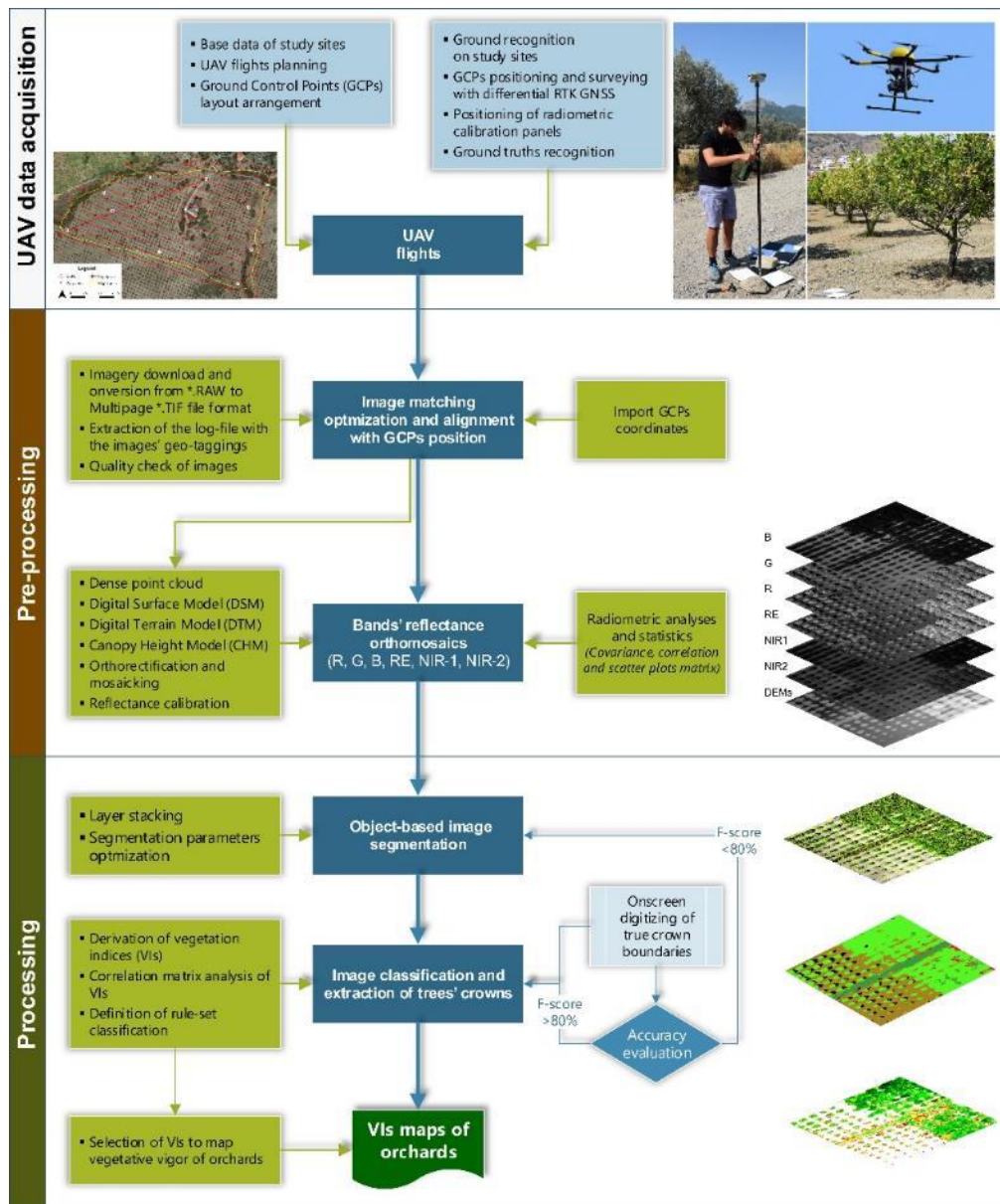


147  
 148 **Fig. 1.** Geographic location and representative photos of the three study sites, A1 (Clementine), A2 (Olive), and  
 149 B (Bergamot and olive) orchard.

150 **3. Materials and Methods**

151 The proposed workflow can be synthesized according to the following methodological steps: UAV data  
 152 acquisition; pre-processing (photogrammetric reconstruction, orthorectification, and mosaicking, radiometric  
 153 and statistical analyses of UAV imagery, derivation of topographic layers); processing (object-based image  
 154 segmentation, derivation of vegetation indices (VIs), image classification and tree crowns extraction,  
 155 accuracy assessment) (Fig. 2).

156



157

158 **Fig. 2** - Workflow of the proposed methodology for the vegetation monitoring at tree crown detail from unmanned  
 159 aerial vehicles (UAVs) multispectral imagery in heterogeneous citrus and olive orchards.

160 **3.1 Surveys Equipment**

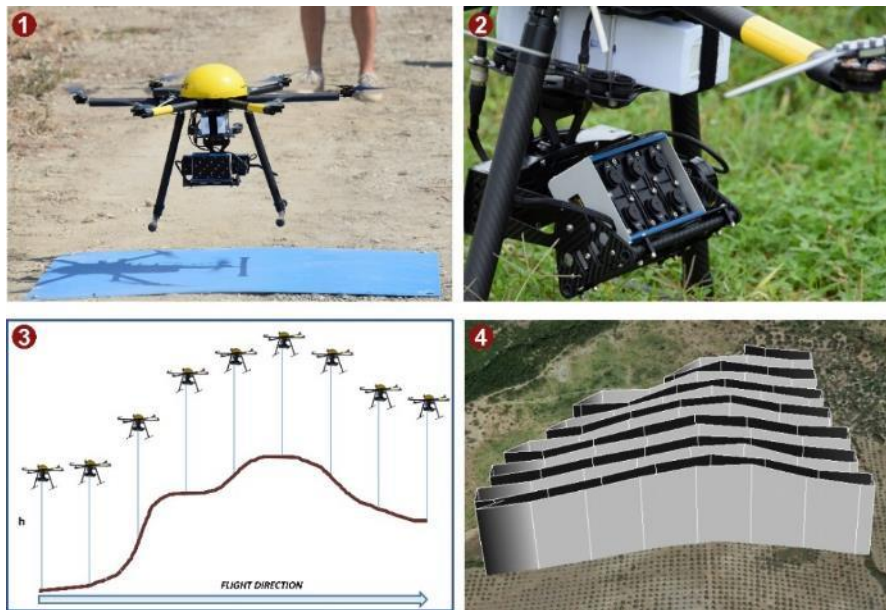
161 UAV surveys were carried out with the Multirotor G4 Surveying-Robot (Service Drone GmbH), a multirotor  
 162 equipped with six high-efficiency electric brushless motors, gimbal and flight control with a dual 32-bit  
 163 processor, able to correct the position 512 times per second of flight, thus ensuring a much more stable flight  
 164 (Fig. 3). The imagery was captured by the  $\mu$ -MCA06 snap, a multispectral camera with a global shutter sensor  
 165 produced by Tetracam Inc. (Chatsworth, USA). The  $\mu$ -MCA06 snap consists of 6 individual 1.3 megapixel  
 166 CMOS sensors (4:3 format, 1280 x 1024 pixels) with interchangeable bandpass filter housed in one unit, one  
 167 named as “master,” responsible for synchronizing the other named as “slaves” (Tab. 1).

168  
169

**Tab. 1.** Tetracam  $\mu$ -MCA06 snap (Global shutter) sensor characteristics bands specification (wavelength and bandwidth).

Geometry of lens	Sensors	Bands	Central band wavelength [nm]	Bandwidth [nm]
Focal Length (fixed lens) 9.6 mm Horizontal Angle of View 38.26° Vertical Angle of View 30.97°  Ground sample distance (GSD) 40.0 mm and field of view (FOV) 51.5 m x 41.25 m at 80 m of flight height	Master (0)	Near-Infrared 1 (NIR1)	800	10
	1	Blue (B)	490	10
	2	Green (G)	550	10
	3	Red (R)	680	10
	4	Red-edge (RE)	720	10
	5	Near-Infrared (NIR2)	900	20

170



171  
172

**Fig. 3.** Upside (1), the UAV Multirotor G4 Surveying-Robot (Service Drone GmbH) equipped with Tetracam  $\mu$ -MCA06 snap multispectral camera; camera mounted on UAV gimbal and ready to capture images (2). Lower side (3), a graphical scheme shows how the UAV takes into account the 3D morphology of the surveyed area, guaranteeing a constant height of flight and (4) a 3D view of a flight plan.

177

178 Each sensor has a dimension of 6.66 mm x 5.32 mm with a pixel size of 4.8 microns and a focal length of  
179 9.6 mm (fixed lens). Images are stored as single shots of 1.3 megapixels per bands, exposing the entire image  
180 at the same instant in time, at either 8 or 10 bit, giving a total of 7.8 megapixels across the six bands. The  $\mu$ -  
181 MCA06 snap was equipped with its own global navigation satellite system (GNSS), the FirePoint 100 GPS.

### 182 3.2 Data acquisition and pre-processing

183 Flight missions were planned with the UAV Planner 3D ([www.alto-drones.com](http://www.alto-drones.com), last access 31 January 2020),  
184 a commercial plugin available for version 2 of QGIS, and that allows us to take into account the 3D

185 morphology of the study area (Fig. 3). All flights were carried out with 80 m above ground level (a.g.l) of  
 186 flight height, a field of view (FoV) of 51.5 x 41.25 m, ground sample distance (GSD) of 4 cm, and with 2.5  
 187 m s<sup>-1</sup> of cruise speed (Tab. 2). To ensure a high quality of the obtained imagery, overlap and side lap were  
 188 set at 80% and 75%, respectively. Within each study site, 50 cm x 50 cm white polypropylene panels and  
 189 covering two quadrants, using black cardboard to locate the point, were used as ground control points (GCPs),  
 190 were distributed. Every GCP was georeferenced in the field, using the Leica GS12 RTK-GNSS, in the  
 191 coordinate system WGS84/ETRF1989 UTM33N (EPSG 32633) (planimetric accuracy ±2.5 cm, altimetric  
 192 accuracy ±5 cm).

193

194 **Tab. 2** - Flight and UAV dataset characteristics.

ID	Date	Flight height [a.g.l.]	Take-off time [UTC+1]	Speed [m s <sup>-1</sup> ]	N° of flights	Total duration [min]	Surveyed area [ha]	Photos [n°]	Overlap [%]	Sidelap [%]	RMSE [m]		
											X	Y	Z
A1	2016/11/16	80 m	12:00	2.5	2	38	4.6	1026	80	75	0.05	0.05	0.08
A2	2017/02/15	80 m	12:00	2.5	2	40	7.12	1878	80	75	0.07	0.07	0.1
B	2018/09/17	80 m	11:00	2.5	2	49	7.9	2825	80	75	0.03	0.03	0.09

195

196 With the aim to calibrate the conversion of the original digital numbers (DN) to band reflectance, three 50  
 197 cm x 50 cm polypropylene calibration panels (in white, black, and grey) were placed on the field. During the  
 198 flight, for each of them, the reflectance was recorded with the Apogee M100 spectroradiometer. The grey  
 199 panel was chosen as reference, and its reflectance value in correspondence of each central band was extracted.  
 200 These values were used, together with radiometric correction parameters written in the EXIF metadata of the  
 201 images, to compute the radiometric calibration of each pixel, allowing to generate the reflectance maps. UAV  
 202 images were acquired in the \*.RAW native format then converted to 10-bit TIFF format using PixelWrench  
 203 II (version 1.2.4, Tetracam, Inc., Chatsworth, USA). Data pre-processing was implemented in Pix4Dmapper  
 204 (Pix4D SA, Switzerland) Pro 4.3 that allows managing the alignment, stacking, and radiometric calibration  
 205 of the original single band images as camera rigs systems. Internal camera orientation was performed based  
 206 on the camera specification and the alignment parameters provided by Tetracam (X and Y translation,  
 207 rotation, and scaling). External orientation was firstly based on the GNSS geotags recorded for each shot and  
 208 further improved through the GCPs positions. Then, classical digital photogrammetry processes based on  
 209 structure from motion (SfM) and aerial triangulation were carried out obtaining sparse and dense 3D clouds,  
 210 digital surface model (DSM), digital terrain model (DTM) and canopy height model (CHM). After the

211 radiometric calibration, a reflectance orthomosaic for each of the six-layer bands was obtained and then  
 212 stacked into a six-band orthomosaic (B, G, R, RE, NIR1, NIR2).

### 213 **3.3 Radiometric analyses and statistics of collected datasets**

214 Before proceeding with image processing, the radiometric characterization of datasets and correlation  
 215 analysis of bands was performed using pairwise scatter plots based on Pearson's correlation coefficient ( $r_{ij}$ )  
 216 according to eq. 1 and organized as scatter plots matrix.

$$217 \quad r_{ij} = \frac{Cov_{ij}}{\sigma_i \sigma_j} \quad (\text{eq. 1})$$

$$218 \quad Cov_{ij} = \frac{\sum_{k=1}^N (DN_{ik} - \overline{DN}_i)(DN_{jk} - \overline{DN}_j)}{N-1} \quad (\text{eq. 2})$$

219 Where  $Cov_{ij}$  (eq.2) is the covariance of layer bands  $i$  and  $j$ ,  $DN_{ik}$  the digital numbers (i.e., the cell value of  
 220 each pixel),  $\overline{DN}_j$  is the mean of the DNs in the specific band ( $i$  and  $j$ ) while  $\sigma_i$  and  $\sigma_j$  are their standard  
 221 deviations calculated as follows (eq. 3).

$$222 \quad \sigma_{i(j)} = \sqrt{\frac{\sum_{k=1}^N (DN_{i(j)} - \overline{DN}_{i(j)})^2}{N-1}} \quad (\text{eq. 3})$$

223 The dataset was analyzed in Python, employing the pandas library and using the rasterio toolbox to read and  
 224 implement the data array of input data. As input data (i.e., the layer bands), we used the six spectral bands B,  
 225 G, R, RE, NIR1, NIR2 plus DSM, and CHM, that we concatenated in a unique data frame through the NumPy  
 226 library. To perform correlation analysis, we used scipy and numpy libraries while the implementation of the  
 227 scatters plots, and the final correlation matrix was based on the matplotlib and seaborn libraries. The graphical  
 228 representation of scatter plots was improved using a kernel density estimation (KDE) with a Gaussian kernel.

### 229 **3.4 Image segmentation**

230 The first phase of a GEOBIA procedure is the segmentation of the original image into separate, non-  
 231 overlapping regions (Aguilar et al., 2016) and extracted as vectorial objects. This process is a fundamental  
 232 pre-requisite for classification/feature extraction (Drăguț et al., 2014). Segmentation consists of the  
 233 partitioning of objects into smaller entities in the creation of new ones and the alteration of the morphology  
 234 of the existing ones according to precise rules. Concerning the approaches in performing the segmentation,  
 235 two different ways are possible: a top-down strategy, which involves cutting large objects into small objects,  
 236 and the bottom-up strategy that merges small objects to form larger ones. In the present research, we adopted

237 a bottom-up strategy, the multiresolution segmentation (Baatz and Schape, 2000), implemented in eCognition  
238 Developer 9.5. Multiresolution segmentation is an optimization process that, for a certain number of image  
239 objects, minimizes the average heterogeneity and maximizes their respective homogeneity (Trimble Inc.,  
240 2019). This algorithm first identifies single objects of the size of a pixel and then merges them with other  
241 neighboring objects according to a criterion of relative homogeneity. This criterion measures the level of  
242 homogeneity within each object. The procedure continues selecting another image object's best neighbor and  
243 proceeds until no further image object mergers can be realized without infringing the maximum allowed  
244 homogeneity of an image object (Trimble Inc., 2019). The result of a good image classification process is  
245 affected mainly by the process quality of segmentation, which in turn depends on the choice of segmentation  
246 parameters values (El-naggar, 2018).

247 Several criteria should be accurately evaluated to obtain proper segmentation (El-naggar, 2018). The  
248 homogeneity criterion derives from the combination of the spectral and shape properties of the initial object  
249 and of that obtained by the merging process. Color homogeneity results from the standard deviation of  
250 spectral colors, while the shape homogeneity derives from the deviation of a compact (or smooth) shape.  
251 Homogeneity criteria can be established by two parameters: shape and compactness. The shape parameter  
252 determines the importance on the segmentation of the shape of the segmented objects with respect to the  
253 color and can assume a value between 0 and 0.9. Shape and color are two interrelated, and their weight is  
254 chosen by the user: the higher the weight of the first, the lower the weight of the second in the segmentation,  
255 and vice versa (Drăguț et al., 2010). Compactness determines the influence of shape respect to the  
256 smoothness. This parameter can be defined by the product of width and length calculated on numbers of  
257 pixels (El-naggar, 2018).

258 Several scholars demonstrated the importance of the scale parameter in determining the final size and  
259 dimension of the resulting objects (Drăguț et al., 2014; Ma et al., 2017). Inserting higher values or smaller  
260 values of scale parameter larger and smaller objects are obtained, respectively. The scale parameter defines  
261 the maximum allowed heterogeneity with regard to the weighted image layers for the obtained image objects  
262 (Trimble Inc., 2019). Therefore, datasets of homogeneous environments will lead to larger segments and vice  
263 versa (El-naggar, 2018). Moreover, in implementing a segmentation process, a different weight can be  
264 assigned to each of the different input data (i.e., band layers). In our proposed workflow, orthoimages were  
265 segmented using a multiresolution algorithm and adopting an equal weight for all band layers. Layers used

266 in this phase were spectral bands B, G, R, RE, NIR1, NIR2, and the DSM in study site A1 while, in the study  
267 sites A2 and B, the NIR2 band has been excluded, considering its very close correlation with the NIR1 band  
268 (0.99). The optimal multiresolution segmentation parameters were obtained by applying a trial-and-error  
269 approach (Aguilar et al., 2016). As reported in Prošek et al. (2019) and Kaufman (1994), the visual  
270 interpretation of segmentation is an effective method to assess the quality of the obtained results. In the study  
271 site A1, segmentation settings were as follows: weight 1 for all layers, scale parameter 60, shape and  
272 compactness 0.1 and 0.5, respectively. In the study site A2, displaying the image in the different band  
273 combinations, and on the basis of a better distinction from the rest of the image of canopies and their own  
274 shadows, a different weight was assigned to the different layers bands. Higher (band weight = 2), for NIR1,  
275 RE, DSM and DTM, lesser (band weight = 1) for B, G and R bands. The scale parameter has been assigned  
276 a value of 200, while the shape and compactness parameters have been assigned a value equal to 0.7. In the  
277 study site B, the segmentation settings were 1, 85, 0.5 and 0.1 for band weights, scale, shape and compactness,  
278 respectively.

### 279 **3.5 Derivation of Vegetation indices (VIs) and topographic elevation layers**

280 A reliable radiometric measurement of vegetation vigor can be obtained combining the information provided  
281 by some specific regions of the electromagnetic spectrum, such as those characterizing the curve between  
282 the maximum absorption of photosynthetic pigments (Jones and Vaughan, 2010). VIs are derived from the  
283 math combination of two or more bands with the aim to obtain useful information on specific vegetation  
284 properties (e.g., chlorophyll) in the R region and the maximum dispersion in RE and NIR regions per single-  
285 pixel (Campbell and Wynne., 2011). VIs, developed since the 1970s (Glenn et al., 2008), have been widely  
286 recognized to have good sensitivity for the detection and monitoring of vegetation (Barrett and Curtis, 2013).  
287 In the present research, six VIs were derived (Tab. 3): normalized difference vegetation index (NDVI),  
288 normalized difference red edge vegetation index (NDRE), soil-adjusted vegetation index (SAVI), green  
289 normalized difference vegetation index (GNDVI), green and red normalized difference vegetation index  
290 (GRNDVI), chlorophyll vegetation index (CVI).

291 In addition, two topographic elevation layers were derived, the DSM (Digital Surface Model) entered as input  
292 while the DTM (Digital Terrain Model) was used to calculate the CHM (Canopy Height Model) (Popescu,  
293 2007). NDVI is one of the most widely used indices derived from the multispectral information and is

294 calculated by the normalized ratio between the Red and NIR bands (Rouse et al., 1974). The index that can  
 295 assumes values between -1 and 1 measures healthy vegetation utilizing the highest chlorophyll absorption  
 296 and reflectance regions and is useful to characterize canopy growth or vigor (Xue and Su, 2017). NDVI is  
 297 very sensitive to background factors, such as the shade and the brightness of the vegetation canopies and soil  
 298 backgrounds. For this reason, Huete (1988) developed the SAVI index with the aim to minimize the effects  
 299 of soil background on the vegetation signal by inserting a constant soil adjustment factor  $L$  in the original  
 300 formula of NDVI (Taylor and Silleos, 2006).  $L$ , which is a function of vegetation density, can assume values  
 301 between 0 and 1, depending on the vegetation amounts. In the presence of shallow vegetation, the value of  $L$   
 302 suggested is 1, while a value of 0.5 is used for intermediate levels of vegetation. Obviously, when the value  
 303 of  $L$  is 0, SAVI corresponds precisely to the NDVI. NDRE has a range of values from -1 to 1 and formula  
 304 similar to that of NDVI but exploits the sensitivity of the vegetation to the RE by replacing the R. GNDVI  
 305 (Gitelson et al., 1996) was proposed using a G band rather than the R band as in the classic NDVI and has  
 306 been developed for the estimation of leaf chlorophyll concentration. CVI (Vincini et al., 2007) was initially  
 307 proposed as a broad-band VI sensitive to leaf chlorophyll content and insensitive to LAI variation. The  
 308 index's formula was obtained from that of green SR multiplying the G/NIR ratio by R/G ratio. R/G ratio,  
 309 developed by Gamon and Surfus (1999), has been used to estimate foliage development in canopies.  
 310 GRNDVI was developed together with a series of indices in whose formulas the R band of NDVI formula  
 311 was substituted with several combinations of R, G, and B bands to verify the response and capability to  
 312 estimate LAI of these indices (Wang et al., 2007).

313

314 **Tab. 3** - Formulation of the six vegetation indices (VIs) used in the present research.

Index denomination	Index formula	References
Normalized Difference Vegetation Index (NDVI)	$\frac{(\rho_{NIR1} - \rho_{Red})}{(\rho_{NIR1} + \rho_{Red})}$	(Rouse Jr. et al., 1974)
Normalized Difference Red Edge Vegetation Index (NDRE)	$\frac{(\rho_{NIR1} - \rho_{RedEdge})}{(\rho_{NIR1} + \rho_{RedEdge})}$	(Barnes et al., 2000)
Soil-Adjusted Vegetation Index (SAVI)	$\frac{(\rho_{NIR1} - \rho_{Red})}{(\rho_{NIR1} + \rho_{Red} + L)}(1 + L)$	(Huete, 1988)
Green Normalized Difference Vegetation Index (GNDVI)	$\frac{(\rho_{NIR1} - \rho_{Green})}{(\rho_{NIR1} + \rho_{Green})}$	(Gitelson et al., 1996)
Chlorophyll Vegetation Index (CVI)	$\rho_{NIR1} \frac{\rho_{Red}}{(\rho_{Green} * \rho_{Green})}$	(Vincini et al., 2007)

Green and Red Normalized Difference Vegetation Index (GRNDVI)	$\frac{\rho_{NIR1} - (\rho_{NIR1} + \rho_{Red})}{\rho_{NIR1} + (\rho_{Green} + \rho_{Red})}$	(Wang et al., 2007)
---	--	---------------------

315 \* $\rho$  is the reflectance at the given wavelength.

316

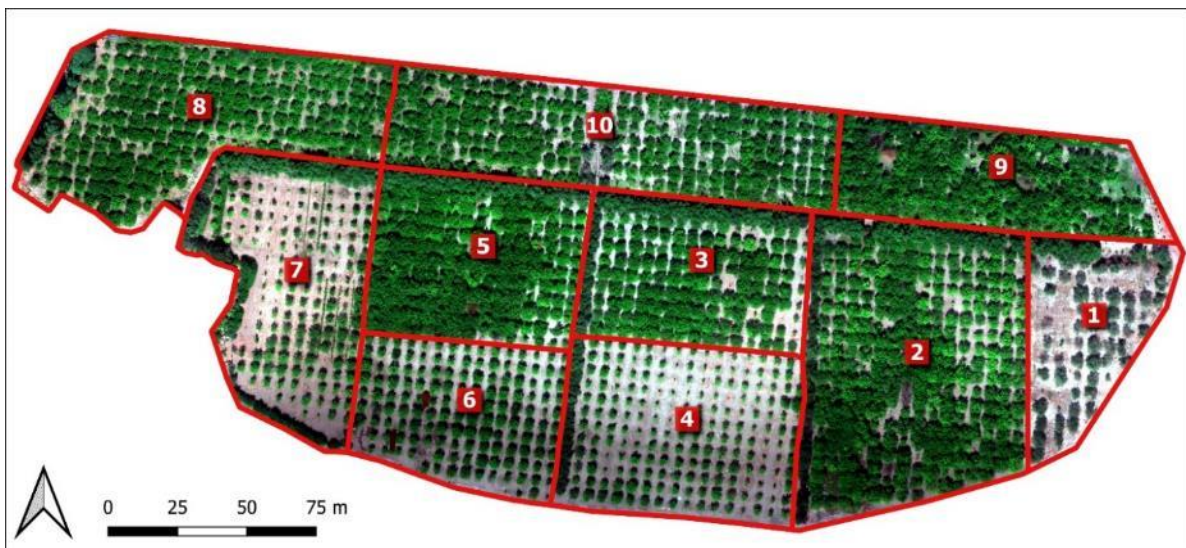
### 317 **3.6 Image Classification and trees' crowns extraction**

318 The classification was based on a rule set implemented in eCognition as an automated process-tree, therefore  
319 adaptable and replicable to other datasets. It was based on the algorithm *Assign Class* that allows assigning  
320 a class to an object which falls within one or more chosen conditions (or rules), based on values attributed to  
321 features (e.g., threshold values of VIs and topographic layers). Therefore, working as a masking-approach,  
322 as shown in De Castro et al. (2018) and Peña-Barragán et al. (2012). In our case, the classification was  
323 performed by assigning, to each target land-use class, different threshold values for each of the different input  
324 layers and VIs (Tab. 4). In the case study A1, the classification was implemented for four classes: “citrus”,  
325 “buildings and roads”, “other vegetation”, and “bare soil”. Being this dataset derived from UAV flights  
326 carried out at midday, and in November, the presence of shadows can be considered as irrelevant. Therefore  
327 it was decided not to create a specific class for these objects. The classification algorithm was set to start with  
328 the class “buildings and roads” using SAVI values  $\leq 0.1$ . “Citrus” were classified using SAVI  $\geq 0.7$  and CHM  
329  $\geq 1.6$ , while “Other vegetation” was classified using CHM values higher than 6. All unclassified objects were  
330 classified as “bare soil”. In the case study A2, the classification was implemented for five classes: “olive”,  
331 “shadows” (due to the different sun position with respect to the horizon line in the month of February),  
332 “buildings and roads”, “other vegetation” and “bare soil”. “Olive trees” were identified using CVI values  
333  $\geq 1.5$  and CHM  $\geq 1.5$ , while “Shadows” were classified using the NIR1 band. “Building and roads” were  
334 classified using SAVI values  $\leq 0.1$  and CHM  $\geq 1.1$ . “Other vegetation” was classified, taking into  
335 consideration their larger canopy size ( $\geq 30 \text{ m}^2$ ) than olive trees. Unclassified objects were inserted in the  
336 class “bare soil”.

337 Also, in the study site B, the classification was implemented for five classes: “Citrus”, “olive”, “shadows”,  
338 “other vegetation” and “bare soil”. Since the citrus orchard is uneven-aged, there were significant differences  
339 in the size of the trees' canopies, we subdivided the image into parcels (Fig. 4). This choice is further justified  
340 by the presence of many olive trees constituting long windbreak barriers in the citrus orchard. Therefore, the  
341 orthomosaic was divided into ten parcels based on the layout scheme of the irrigation sectors that roughly

342 correspond to the different plantation age of bergamot trees. In detail, in sectors 4-6 and 7, trees are 5 years  
343 old. This operation was performed using the open-source software QGIS, creating a specific thematic layer  
344 subsequently imported in eCognition. For this study site, using threshold values of SAVI between -0.16 and  
345 0.45, all the vegetation, without distinguishing between the two species present (olive and bergamot), was  
346 inserted in a temporary class called “vegetation”. In sectors 1 to 5 and 7, characterized by the presence of  
347 olive trees, these were identified using DSM and  $NDVI \geq 0$  and  $CVI \geq 1.3$ , reclassifying the above-mentioned  
348 class. The remaining objects belonging to this class were reclassified as “Citrus”. Anything object that did  
349 not belong to the temporary class “vegetation”, was classified as “bare soil”. Finally, by establishing a  
350 threshold value in the NIR1 band, from the three classes “bare soil”, “olive” and “citrus”, we extracted those  
351 objects belonging to the “shadows” class.

352



353

354 **Fig. 1** - Map showing the study site B with, highlighted in red, the ten parcels identified according to the irrigation  
355 scheme arranged for the bergamot orchard.

356

### 357 **3.7 Accuracy assessment**

358 The approach used in this work was based on the comparison of the total number of correctly detected crown  
359 pixels by classification algorithm with a reference vector data. The reference segments for each image were  
360 manually digitized by on-screen photointerpretation from UAV true-color orthophotos. Differently to other  
361 research works (Ok et al., 2013; Solano et al., 2019; Koc-San et al., 2018), to obtain a comprehensive picture  
362 of the implemented approach, we digitized all the trees' crowns following in the three analyzed study sites.

363 The evaluation metrics used in this work were described and used in several previous studies, each of which  
 364 has given different descriptions. This aspect had already been clarified by Shufelt (1999) and Ok et al. (2013)  
 365 which said that the specific definitions of this approach are subject to varying interpretations. Some of these  
 366 works used an approach object-based (Ok et al., 2013; Ok and Ozdarici-Ok, 2018; Ozdarici-Ok, 2015; Solano  
 367 et al., 2019) in which the validation took place by means of an overlap percentage threshold between the  
 368 image objects, classified by the algorithm, and the reference segments. In these researches, the object-based  
 369 evaluation approach was used in cases where the objects were clearly separable from each other and had  
 370 well-defined edges. In our case, to cope with the heterogeneity of the tree crowns structure in some parts of  
 371 the images, a pixel-based accuracy assessment was implemented. Superimposing trees' crowns with the  
 372 reference vector data, each pixel into one of the three distinct accuracy categories defined below (Goutte and  
 373 Gaussier, 2005; Ok et al., 2013; Shufelt, 1999; Sokolova et al., 2006):

- 374 – True Positive (TP): when a pixel is labeled as a *tree* by the classification algorithm and corresponds to a  
 375 *tree* in the reference vector data (pixel correctly classified).
- 376 – False Negative (FN): when a pixel is labeled in the reference vector data as a *tree* but it not labeled as a  
 377 *tree* by the classifier (pixel not detected).
- 378 – False Positive (FP): indicates a pixel labeled as a *tree* by the classifier, but that does not correspond to  
 379 any of the pixels labeled by the reference vector data (pixel erroneously detected).

380 To evaluate the accuracy, the number of TP, FP, and FN pixels were counted for each image. Then the *Recall*  
 381 (*r*), *Precision* (*p*), *F-score* (*F*) and *Branching Factor* (*BF*) metrics are computed, using the following  
 382 equations (eq. 4-5-6-7) (Goutte and Gaussier, 2005; Li et al., 2012; Ok et al., 2013; Shufelt, 1999; Sokolova  
 383 et al., 2006):

$$384 \quad r = \frac{\| TP \|}{\| TP + FN \|} \quad (\text{eq. 4})$$

$$385 \quad p = \frac{\| TP \|}{\| TP + FP \|} \quad (\text{eq. 5})$$

$$386 \quad F = 2 \cdot \frac{r \cdot p}{r + p} \quad (\text{eq. 6})$$

$$387 \quad BF = \frac{\| FP \|}{\| TP \|} \quad (\text{eq. 7})$$

388 The *r* parameter, measuring the fraction of pixels that were correctly denoted as object pixels by the  
 389 algorithm, allows to represents the omission error (derived from  $1-r$ ). The parameter *p* is indicating the  
 390 correctness of detected crowns, and then, in the same way, it is representative of the commission error

391 ( $1-p$ ).  $F$  measures the overall accuracy through the harmonic mean of commission and omission errors. The  
392 values of  $r$ ,  $p$ , and  $F$  vary from 0 to 1. In order to obtain a higher  $F$ , both  $r$  and  $p$  should be high. For example,  
393 if all of the trees are correctly segmented, the values of  $r$  and  $p$  are 1, resulting in  $F$  being equal to 1 (Goutte  
394 and Gaussier, 2005; Li et al., 2012; Shufelt, 1999; Sokolova et al., 2006). The  $BF$  is a measure of the degree  
395 to which an algorithm over classifies background pixels with the target label (i.e., tree crown in our case). If  
396 the classifier never “over-delineates” the extent of any reference segment, its branching factor value is 0. If  
397 every classified pixel in the image scene is wrongly labeled, the  $BF$  is equal to 1 (Shufelt, 1999). All these  
398 measures taken together give a clear and objective picture of a classification algorithm performance (Shufelt,  
399 1999).

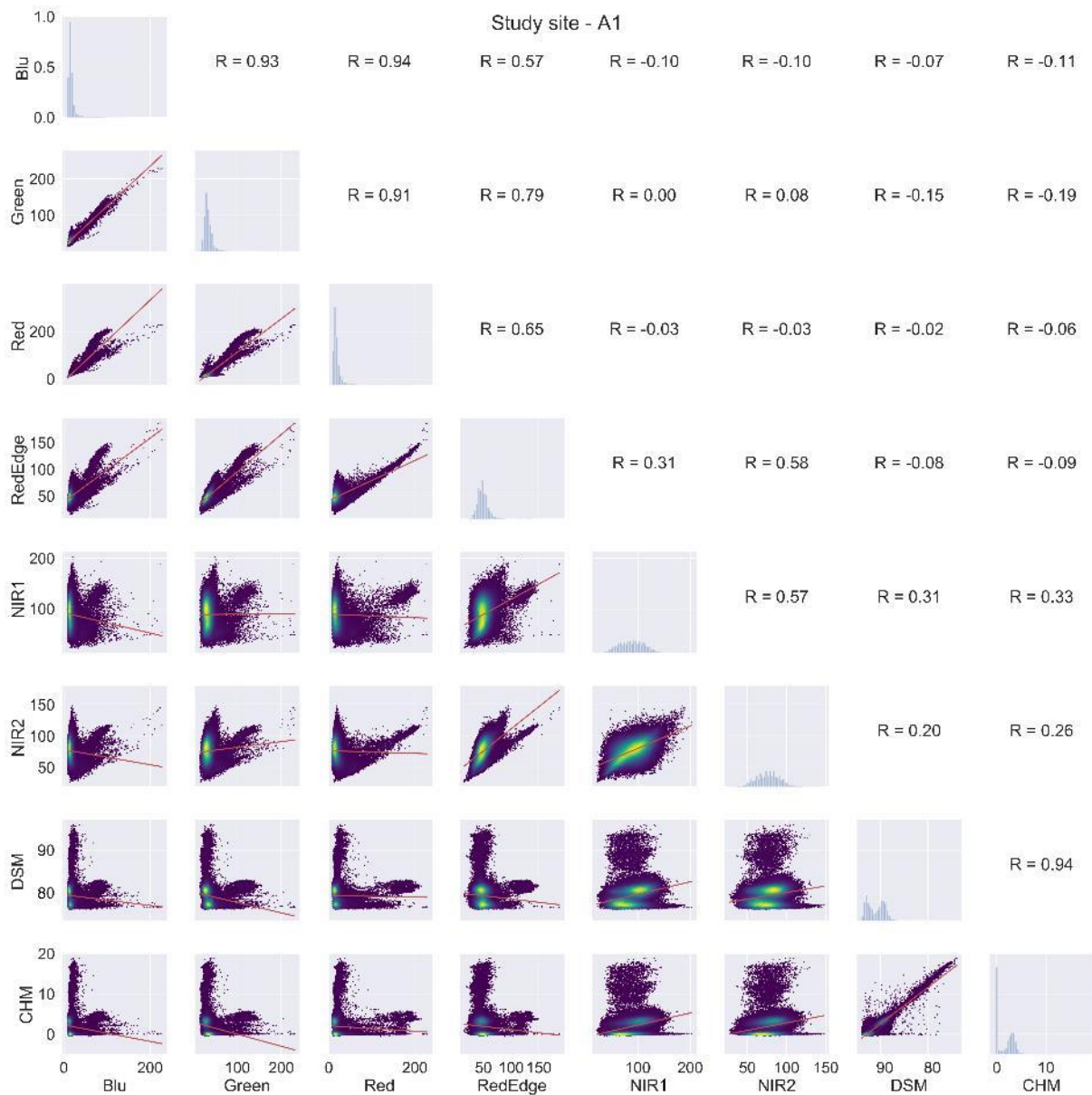
## 400 **4. Results and discussions**

### 401 **4.1 Geometric and radiometric characteristics**

402 All consecutive images of the three datasets were processed via aerial image triangulation with the geo-  
403 tagged flight log and the GCPs’ coordinates through the software Pix4D Mapper. 3D densified point clouds,  
404 DSM, DTM, and for each band reflectance orthomosaics for each spectral band were generated. For DSM  
405 and orthomosaics, the obtained GSD was comprised between 4.1 and 4.3 cm pixel<sup>-1</sup>. As far as the method  
406 applied in the three datasets is concerned, the scenario is different, prior to proceeding with the classification  
407 step, for each study site, a correlation analysis between all input layers was performed through the Pearson’s  
408 correlation coefficient ( $r_{ij}$ ) and implemented in a scatter plots matrix (Figg. 5, 6 and 7). Moreover, to have a  
409 comprehensive view of the spectral correlation between the six derived VIs, we analyzed it on the whole  
410 datasets as a correlation matrix (provided as supplementary material).

411 Referring to the whole datasets, in the study site A1 (Fig. 5), high correlations of SAVI with NDVI (0.99),  
412 GNDVI (0.95), and GRNDVI (0.98) were evident. SAVI was very important in the classification of  
413 “buildings and roads” and then for classification of the “citrus trees” class, coupled with the CHM, and using  
414 a threshold value  $\geq 0.7$ . NDRE showed a high correlation with GNDVI (0.89) and low correlations with  
415 NDVI (0.77), SAVI (0.77), and CVI (0.78).

416



417

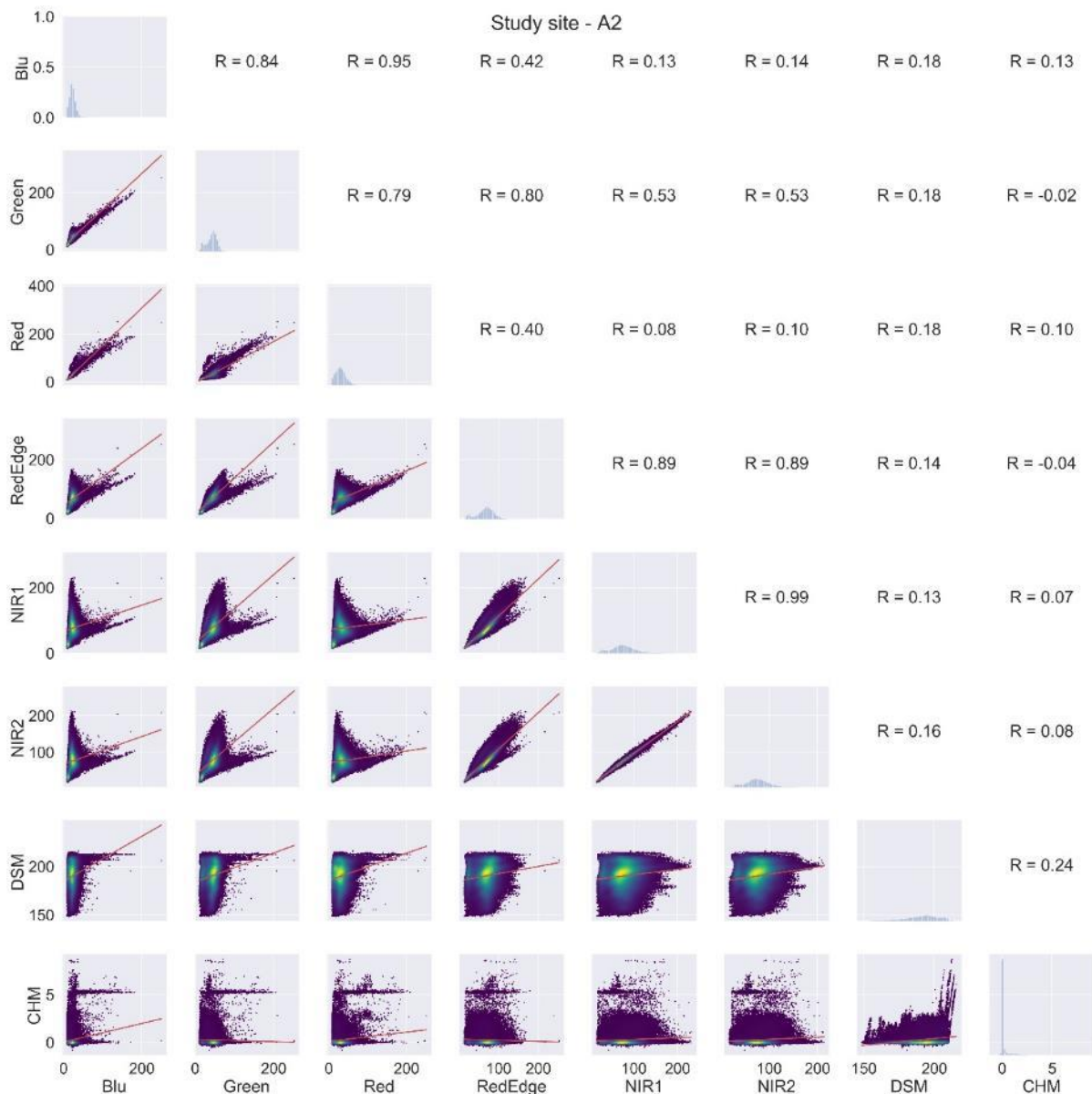
418

419 **Fig. 5** – Study site A1. Scatter plot matrix showing all bivariate relationships between the input layer bands. For  
 420 each scatterplot, implemented using the 2D kernel density estimate (KDE) with a Gaussian function, the  
 421 correlation line (in red) was provided. The main diagonal reports the histograms showing the frequency distribution  
 422 of pixel values. In the upper half-matrix, Pearson’s correlation (R) coefficients for all pairwise combinations of  
 423 variables are reported.

424

425 Observing correlation matrices on input data of the study site A2 (Fig. 6), there were evident high correlations  
 426 between the NIR bands and the RE (0.88) and between the two NIR bands (0.99). This last significant  
 427 correlation led to the choice to exclude the NIR2 band as an input layer from the segmentation phase onwards.

428



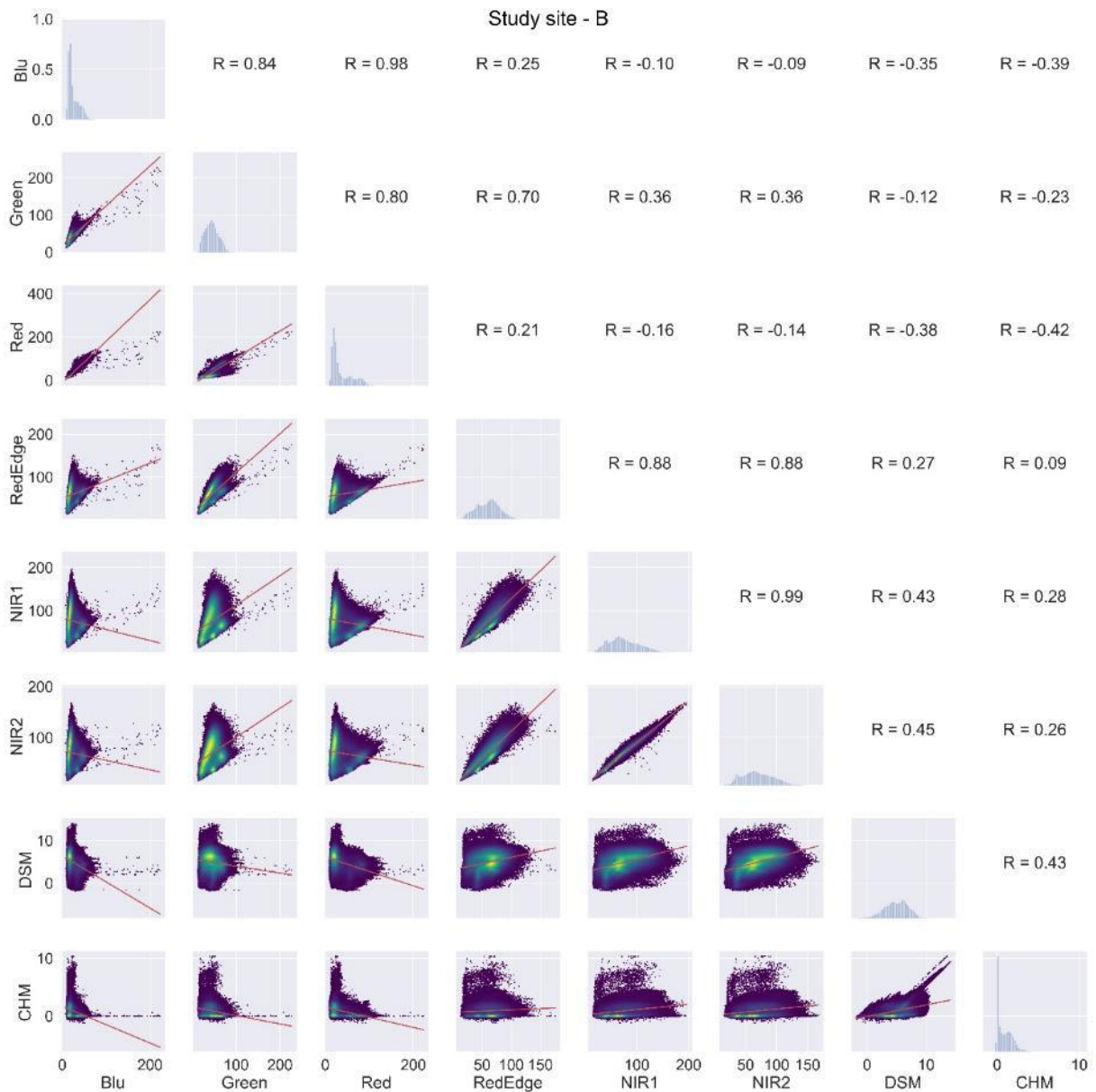
429

430

431 **Fig. 6** - Study site A2. Scatter plot matrix showing all bivariate relationships between the input layer bands. For  
 432 each scatterplot, implemented using the 2D kernel density estimate (KDE) with a Gaussian function, the  
 433 correlation line (in red) was provided. The main diagonal reports the histograms showing the frequency distribution  
 434 of pixel values. In the upper half-matrix, Pearson's correlation (R) coefficients for all pairwise combinations of  
 435 variables are reported.

436

437 In study site B (Fig. 7), examining the correlations of the input data, it is possible to highlight a high  
 438 correlation between NIR and RE bands (0.88) and between the two NIR bands (0.99). Also, for this study  
 439 site, the NIR 2 band was excluded as an input layer from the segmentation phase onwards. As far as the VIs  
 440 are concerned, the correlation of SAVI was very high with GRNDVI (0.96) and NDVI (0.99), while there  
 441 was no significant correlation of CVI with others VIs.



443

444

445 **Fig. 7 -** Study site B. Scatter plot matrix showing all bivariate relationships between the input layer bands. For  
 446 each scatterplot, implemented using the 2D kernel density estimate (KDE) with a Gaussian function, the  
 447 correlation line (in red) was provided. The main diagonal reports the histograms showing the frequency distribution  
 448 of pixel values. In the upper half-matrix, Pearson’s correlation (R) coefficients for all pairwise combinations of  
 449 variables are reported.

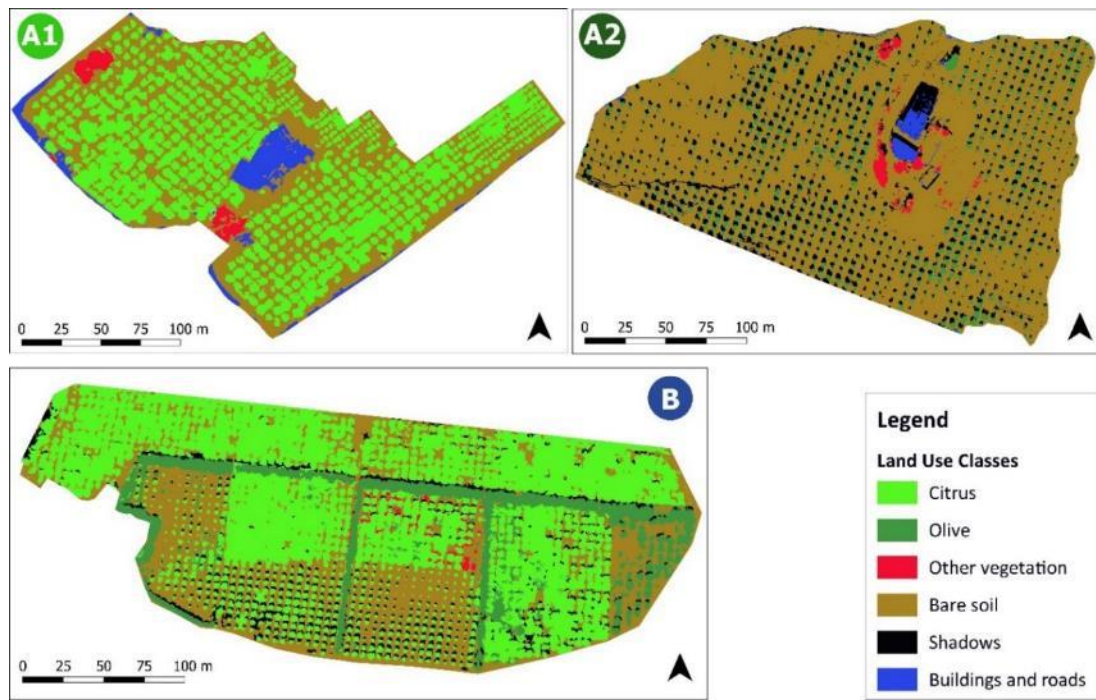
450

451 CVI and SAVI were essential for the correct classification of the olive and bergamot species. NDRE showed  
 452 a high correlation with GNDVI (0.93), NDVI (0.86), and SAVI (0.86).

453

454 **4.2 Image classification, tree crown extraction and accuracy assessment**

455 The image classification was based on six land use classes, “citrus”, “olive”, buildings and roads”, “other  
456 vegetation”, “bare soil” and “shadows” (Fig. 8). In the study site A1, the identification of the class “buildings  
457 and roads” allowed to isolate from the rest of the image elements of no interest using SAVI. For the trees’  
458 classification, the minimum height of the objects was identified by means of verification of CHM’s values.  
459 All trees were included in the “citrus” class by combining the SAVI index with CHM. The third class created,  
460 called “other vegetation”, included different tree species, distinguishable from citrus trees, as they are larger  
461 in canopy size. Other vegetation was identified based on CHM values higher than those used for citrus trees  
462 class. The part of the image excluded from the first three classes was assigned to the class “Bare soil”.  
463



464  
465 **Fig. 8** - Land use maps of the three study sites obtained applying the implemented image object classification  
466 workflow. A1(Clementine), A2 (Olive), and B (Bergamot and Olive).

467  
468 In the study site A2, the classification of “Olive trees” was performed using CVI combined with CHM in  
469 order to avoid the attribution of the class to some specific regions of grass sensitive to the used VI. About  
470 “Shadows”, the use of the NIR1 band allowed to easily classify them, while “Building and roads” were  
471 isolated from the rest of the image by combining the CHM with the SAVI. In the case of “Other vegetation”,

472 this class was easily identified based on a larger canopy size than the elements classified in “Olive trees”.

473 Unclassified objects were included in the class “Bare soil”.

474 The dataset B was the most complex, and the largest of the three analyzed study sites and is occupied by two

475 species (olive and bergamot) that coexist in several parts of the orchard. Olive trees can be found separately

476 from the bergamot orchard at the right end of the image, while in the remaining part, they act as a windbreak.

477 The latter are not of the same age and consequently have different heights and sizes of the canopies. The

478 same trees were not properly pruned, and, as a result, most of the canopies of larger trees touch on one or

479 more sides. On the contrary, there are small trees (especially in the sectors 4-6 and 7) whose canopies reveal

480 relevant portions of bare soil. Given this situation of heterogeneity characterizing the entire image in different

481 aspects, it was decided to subdivide it by grouping the bergamot trees based on the layout scheme of the

482 irrigation sectors that roughly correspond to the different plantation age. The differences in height between

483 the trees within the individual sectors led to the decision to classify only using VIs. Initially, the entire tree

484 vegetation was classified without distinction of species, using a temporary class, “Vegetation class”,

485 operating by sectors with different threshold values of SAVI. Depending on the presence of bare soil or grass,

486 a value of 1 or 0, respectively, was set as factor L in SAVI’s formula. Then, the isolation of the olive trees

487 from the rest of the orchard’s trees was done using the SAVI ( $L=1$ ) in the sector (1) where olive trees have a

488 regular plantation scheme and the CVI where olive trees served as a windbreak barrier (2-5, and 7).

489 The proposed method, tested on the three datasets, is based mainly on the identification of characteristics of

490 spectral response that allows enhancing the detection and classification of an object of interest (citrus trees

491 in dataset A1, olive trees in dataset A2, and both species in dataset B). Further measures could provide useful

492 information on the classification step but were not considered since, as explained, for example, in Laliberte

493 and Rango (2009), it is time-consuming to compute several features during the object-based analysis. This

494 method, which has proved effective in datasets of different complexity, finds its strong point is the speed of

495 execution and on its repeatability to other different crops with few adjustments. As far as the processing

496 speed is concerned, the net of the time needed to obtain the orthomosaics, the time is taken in total for the

497 three datasets, was 4 hours. Of which one hour was used for each of the first two datasets, A1 and A2,

498 including visual analysis of images, followed by segmentation and classification. The remaining time was

499 requested by the dataset B. Indeed, the time requested for the manual digitizing of the reference canopies

500 (explained below), and for the verification of the accuracy of the results, is not added to the total computation

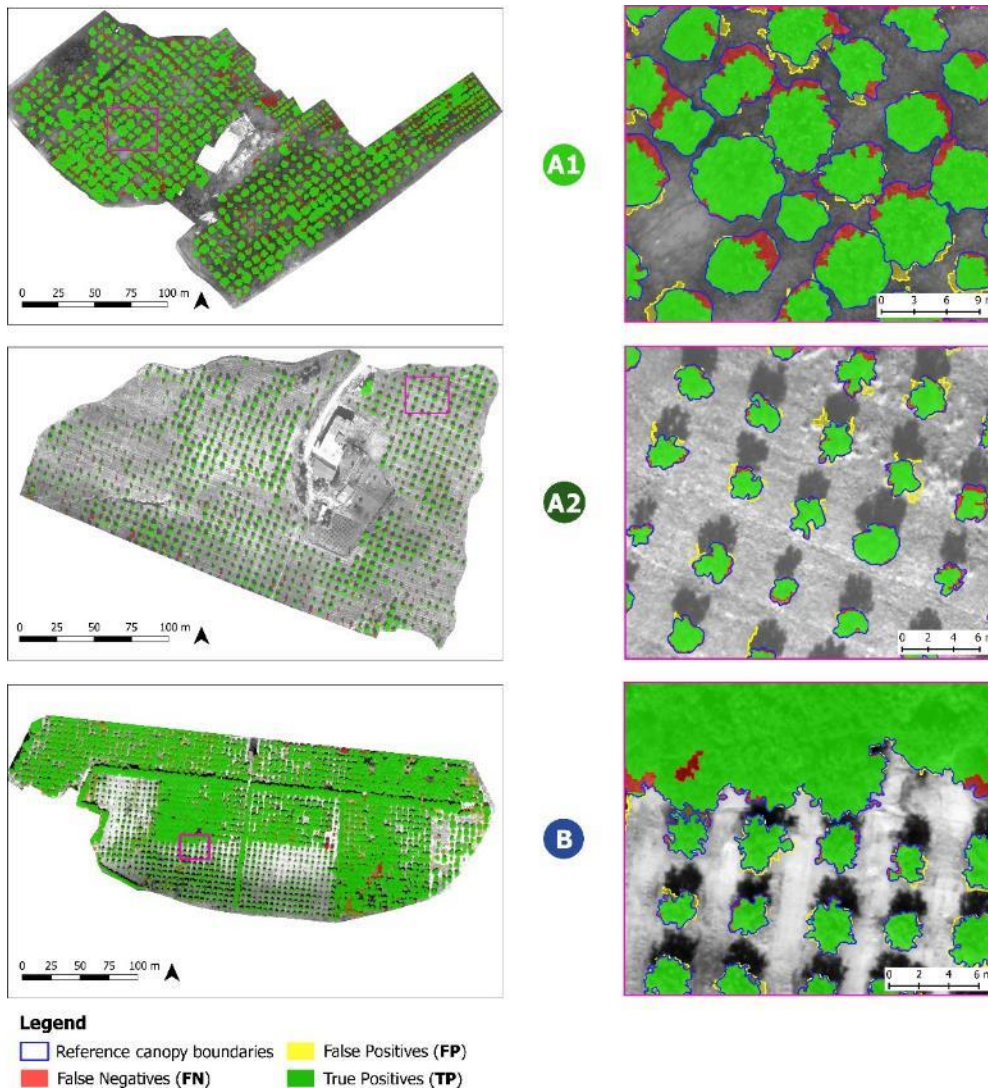
501 time of the entire process. As for the repeatability of the proposed method in other contexts, it is worthy of  
502 interest to consider the obtained accuracy on the three datasets in the crown extraction phase. Results showed  
503 that most of olive and bergamot's trees were correctly classified and extracted in all the three analyzed study  
504 sites. .

505 Concerning the obtained accuracy, Fig. 9 shows the extracted trees when they were overlaid on the reference  
506 data, and provided for each dataset. The green color (TP) indicates the correctly detected trees' crowns  
507 according to the manual digitization, and that represents the reference data. The yellow color (FP) denotes  
508 crowns that were found by the algorithm, where there was no tree in the reference data. The red color (FN)  
509 represents missing crowns, i.e., where the algorithm did not detect tree canopies or parts of trees, and which  
510 were instead present in the reference data. As can be found analyzing the results reported in Tab. 4, in study  
511 site A1, the value of  $r$  (omission error) is 0.80, while the  $p$  value (commission error) is 0.94. The  $F$  that takes  
512 into account both  $r$  and  $p$  is 0.86. In the study site A2, where the classification concerned only olive trees,  $r$   
513 is 0.81, and  $p$  is 0.89., while the  $F$  is 0.85. In the study site B, the values of  $r$ ,  $p$ , and  $F$  are 0.96 ( $F$ -score of  
514 bergamot trees is 0.91 and that of olive trees 0.85), 0.84 and 0.90, respectively.

515 Analyzing the precision in identifying and extracting the trees' canopies, the best results in terms of  
516 percentage of  $TP$  pixels and  $F$ , among all the three analyzed datasets, were obtained in the study site B  
517 (81.66% and 0.90, respectively). The percentage of FP was also the highest of the three datasets (15.22%)  
518 and is mainly found in zones where there was a short distance between canopies, and there was, at the same  
519 time, a thick layer of grass. The percentage of FN was the lowest (3.12%) concerning the failure of the  
520 classifier in identifying parts of canopies and some trees on edge the image, at the top of the image, where  
521 there is, of course, a distorting effect, and some trees in sector 3, where some tiny trees can be found.

522  $FN$  pixels represent 18.5% and 16.65% in the study sites A1 and A2, respectively. This is due to both the  
523 sporadic presence of canopies identified by the classifier and the error caused by the surrounding grass of  
524 background in identifying the canopy along the edges. As shown in Koc-San et al. (2018), it is difficult when  
525 the background's spectral values are similar to those of trees (i.e., grass). Moreover, in the study site A2,  
526 considering the parameters used for the classification ( $CHM > 1.5$  and  $CVI > 1.5$ ), tiny olive trees with a low  
527 vegetation vigor, were not correctly identified and classified.

528 Given the complexity and heterogeneity of the classified orchards and considering that we adopted a pixel-  
529 based accuracy assessment, the obtained results can undoubtedly be considered as very satisfactory.



531

532

533 **Fig. 9** – Maps showing a visual picture of the obtained accuracy in the analyzed three study sites [A1 (Clementine),  
 534 A2 (Olive) and B (Bergamot and Olive)], using the onscreen digitized canopy boundaries as reference data.  
 535 Reference crowns (Rc) are in blue, true positives (TP) are in green, false negatives (FN) in red, and false positives  
 536 (FP) in yellow.

537

538 **Tab. 4** - Results and accuracy indicators of the trees' crowns extraction (TP, true positives; FP, false positives;  
 539 FN, false negatives; r, recall; p, precision; branching factor, BF).

Study site	*TP	*FP	*FN	r	p	BF	F-score
A1	5,600,825 (76.75%)	345,273 (4.75%)	1,350,538 (18.5%)	0.80	0.94	0.06	0.86
A2	2,093,729 (74.25%)	256,891 (9.10%)	470,206 (16.65%)	0.81	0.89	0.12	0.85
B (Bergamot)	10,018,331 (83.3%)	1,612,542 (13.4%)	397,518 (3.3%)	0.96	0.86	0.16	0.91
B (olive)	2,021,941 (74.47%)	631,225 (23.25%)	61,879 (2.28%)	0.97	0.76	0.31	0.85
<i>B (overall)</i>	12,040,272 (81.66%)	2,243,767 (15.22%)	459,397 (3.12%)	0.96	0.84	0.18	0.90

540

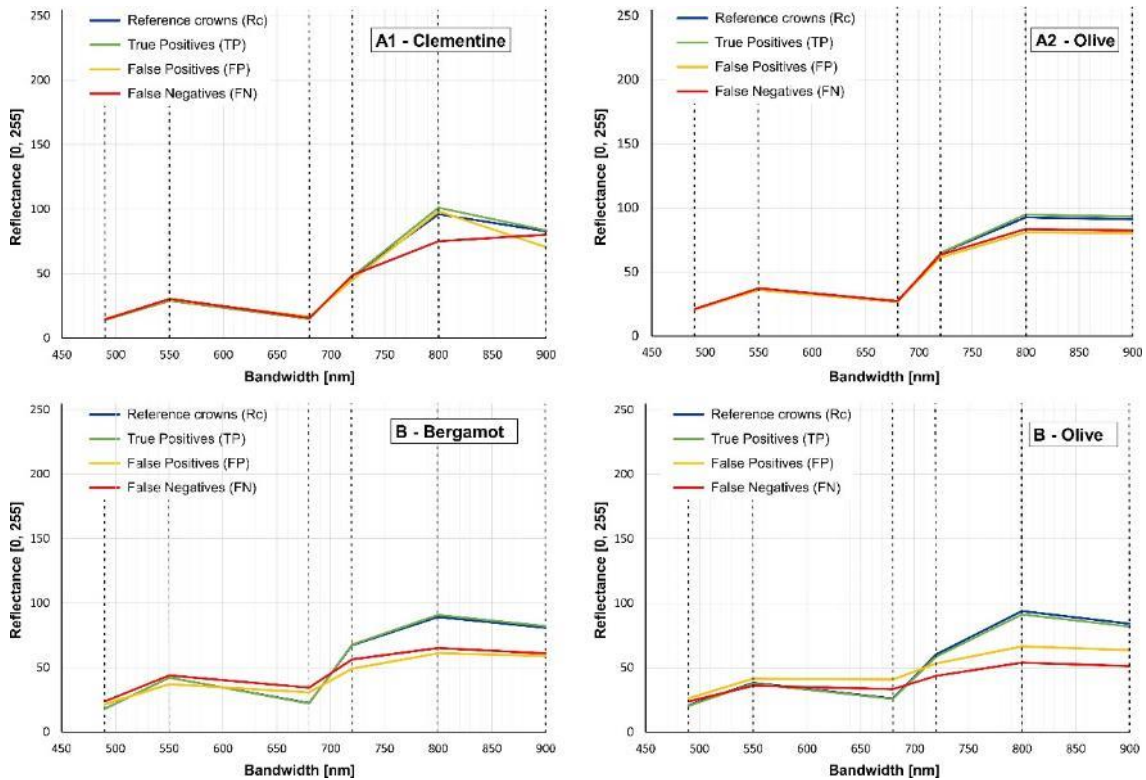
\* TP, FP, and FN are expressed in numbers of pixels.

541  
542  
543  
544  
545  
546  
547  
548  
549  
550  
551  
552  
553  
554  
555  
556  
557  
558

Moreover, it appears worth of interest to highlight that the TP category (i.e., crowns correctly detected and extracted), contains only pixels correctly classified, differently from an object-based accuracy assessment. In this latter case, all polygons, whose overlap area with the reference area is higher than a minimum threshold value (i.e., Ok and Ozdarici-Ok, 2018; Rutzinger et al., 2009), are classified as TPs, therefore also containing pixels not correctly classified. Moreover, also referring to the F-score observed in the study site A2 (0.85), and comparing these results with those reported by other scholars (Ok and Ozdarici-Ok, 2018; Ozdarici-Ok, 2015), in more regular and well-managed orchards, our results can be considered very promising. The same consideration can be made by comparing the results of this work with those obtained by using other methods including convolutional neural networks, LiDAR's data and algorithms based on the use of DSMs (Csillik et al., 2018; Li et al., 2012; Mohan et al., 2017; Ok and Ozdarici-Ok, 2018).

On the other hand, the results obtained in study site B (the more complex among the three analyzed), with an overall F-score of 0.90 and with an FN comprised between 2.28% and 3.3%, strongly corroborated our proposed methodology. Our results suggest that our proposed workflow can allow us to classify and extract trees' crowns in an easier, faster, and more effective way in well-managed orchards.

To better understand the results of the trees' canopy extraction, we analyzed the average spectral profile of reference crowns (Rc), TP, FP, and FN (Fig. 10).



559

560 **Fig. 10** - Meanspectral profiles of reference crowns (Rc) (in blue), true positives (TP) (in green), false negatives  
 561 (FN) (in red), and false positives (FP) (in yellow) in the analyzed three study sites, A1 (Clementine), A2 (Olive)  
 562 and B (Bergamot and Olive).

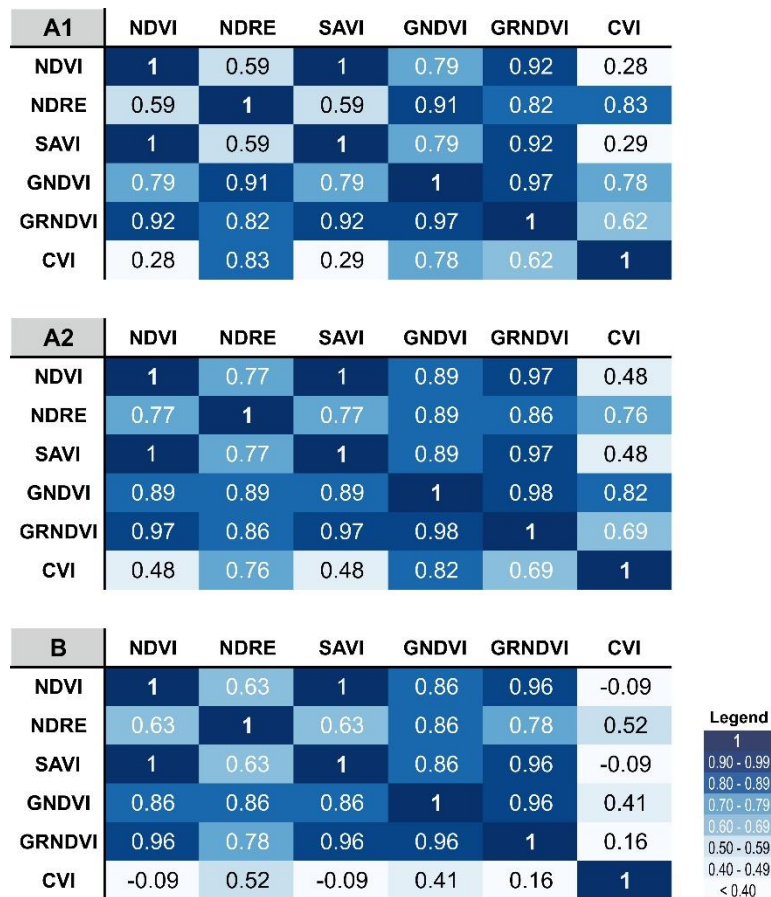
563

564 In study site A1, FP has the same mean radiometric profile of TP and Rc, while TP differs only in the NIR1  
 565 band. Similarly, in the study site A2, the spectral behavior of FN and FP is the same and very near to that of  
 566 TP and Rc. Therefore, these objects were easily misclassified. Analyzing the mean spectral behavior in the  
 567 study site B, the situation is quite different. FN and FP have the same spectral behavior but further to that of  
 568 TP and Rc, compared to study sites A1 and A2. Several of them are located where the bergamot and olive  
 569 tree canopies touch each other and on the border of the study side, where the number of overlapping images  
 570 of the orthomosaic was lower than the rest of the image.

### 571 **4.3 Vegetation indices (VIs) and vigor maps**

572 Vigor maps were produced after a correlation analysis of the six VIs and only referring to olive and citrus  
 573 trees (Fig. 11).

574



575

576 **Fig. 11** - Correlation matrix between the six selected vegetation indices (VIs) implemented only using the class of  
577 trees (bergamot, clementine, and olive) as input data.

578

579 For each study site, two vigor maps were produced (Figs. 12 and 13). Observing correlation matrices on VIs  
580 applied on trees' crowns in the study case A1, a high correlation there was between, GNDVI and GRNDVI  
581 (0.97), GNDVI and NDRE (0.91) while the correlation is not very high between GNDVI and NDVI (0.79).  
582 NDVI corresponds to SAVI (1) but is low correlated with NDRE (0.59). For these reasons, NDRE and N  
583 were chosen for the production of vigor maps of the orchards.

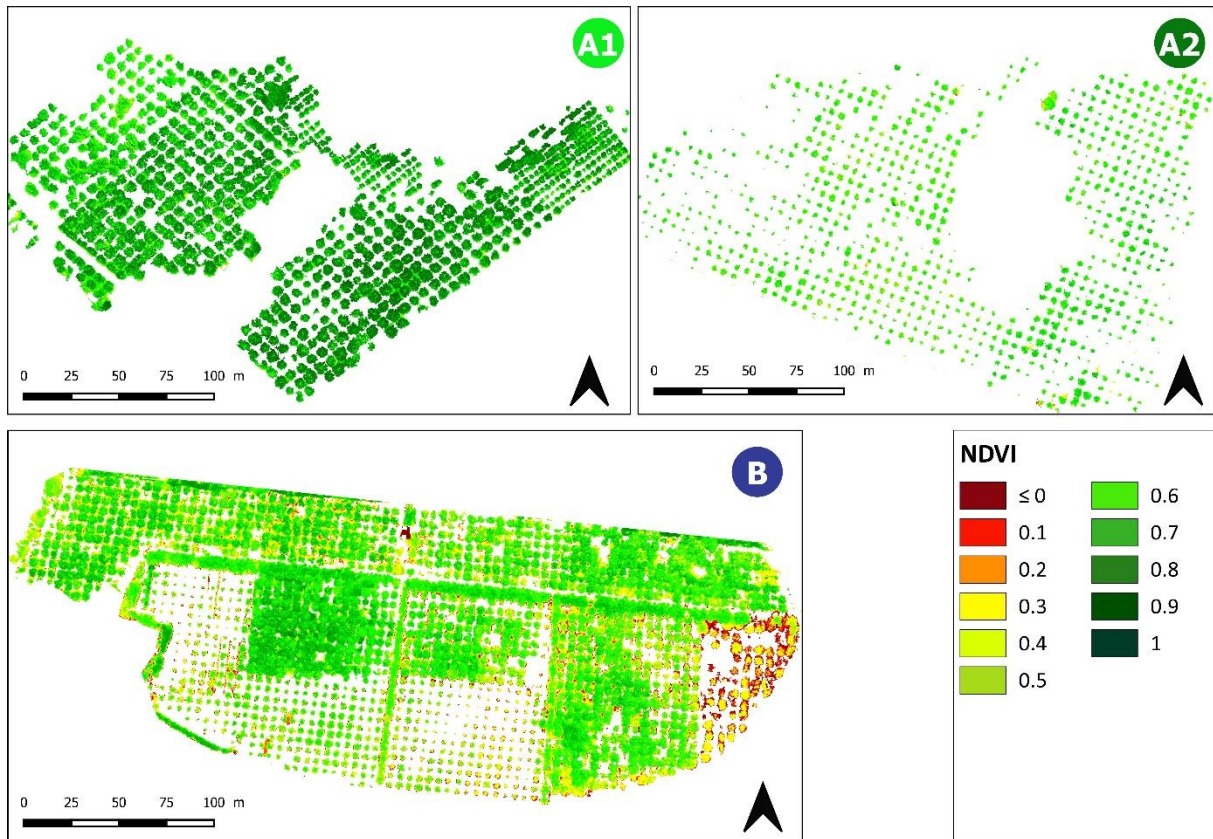
584 In the study-site A1, the NDVI map (Fig. 12) highlights the presence of two distinct zones of the citrus  
585 orchard. One where the clementine trees show a reduced vegetative vigor and with index values ranging  
586 between 0.4 and 0.65 and one with NDVI values, comprised between 0.7 and 0.9, shows a better tree vigor.  
587 NDRE (Fig. 13) takes average vigor values between 0.2 and 0.3 in most parts of the citrus orchard. The  
588 lowest values, highlighted in red in the vigor maps (Figs. 12 and 13), are found where, being the foliage less  
589 dense, the soil of the background appears.

590 As for the case study A2 observing correlation matrices on VIs applied on trees' crowns, there were evident  
591 high correlations between the NDVI, GNDVI, and GRNDVI. At the same time, SAVI and CVI had no  
592 significant correlations with the other VIs. The olive orchard was classified using the CVI coupled with  
593 CHM, as in the case of study site A1, while shadows and buildings were identified using the NIR band and  
594 the SAVI coupled with the CHM. GNDVI was a good correlation with NDRE (0.89), NDVI (0.89), SAVI  
595 (0.89), and a very high correlation with GRNDVI (0.98). SAVI was a high correlation with GNDVI (0.89)  
596 and GRNDVI (0.96) and NDVI (1). NDRE showed a high correlation with GNDVI (0.89) and low  
597 correlations with NDVI (0.77), SAVI (0.77), and CVI (0.76). As in the previous dataset, NDRE and NDVI  
598 were chosen to map vigor in this study site.

599 The NDVI vigor map (Fig. 12) showed that the vegetative status of the olive grove is not good, with values  
600 ranging from 0.15 to 0.7. Therefore, highlighting the vegetative stress of this orchard, planted in unsuitable  
601 land characterized by a very clayey and compact soil. The NDRE vigor map (Fig. 13), on the other hand,  
602 assuming low to medium values, ranging between 0.2 and 0.3, confirms what has already been highlighted  
603 by the NDVI index.

604 Considering correlation matrices on VIs applied on trees' crowns in case study B, similar correlations to  
605 those concerning the indices applied on the entire scene were verified with regard to the NDVI, but there is  
606 an apparent low correlation between NDRE and NDVI (0.63). Therefore these two indices were chosen to  
607 map vigor. The NDVI vigor map (Fig. 12) still proves to be suitable for monitoring the health status of the  
608 vegetation. In particular, in the lower part of the image and on the right, where both bergamot and olive trees  
609 are closer to the sea, and where the vegetative vigor is lower than the rest of the image, the NDVI assumed  
610 values between 0.15 and 0.5. The highest values, as well shown on the map, can be found in sector 5, with  
611 values comprised between 0.75 and 0.9.

612



613

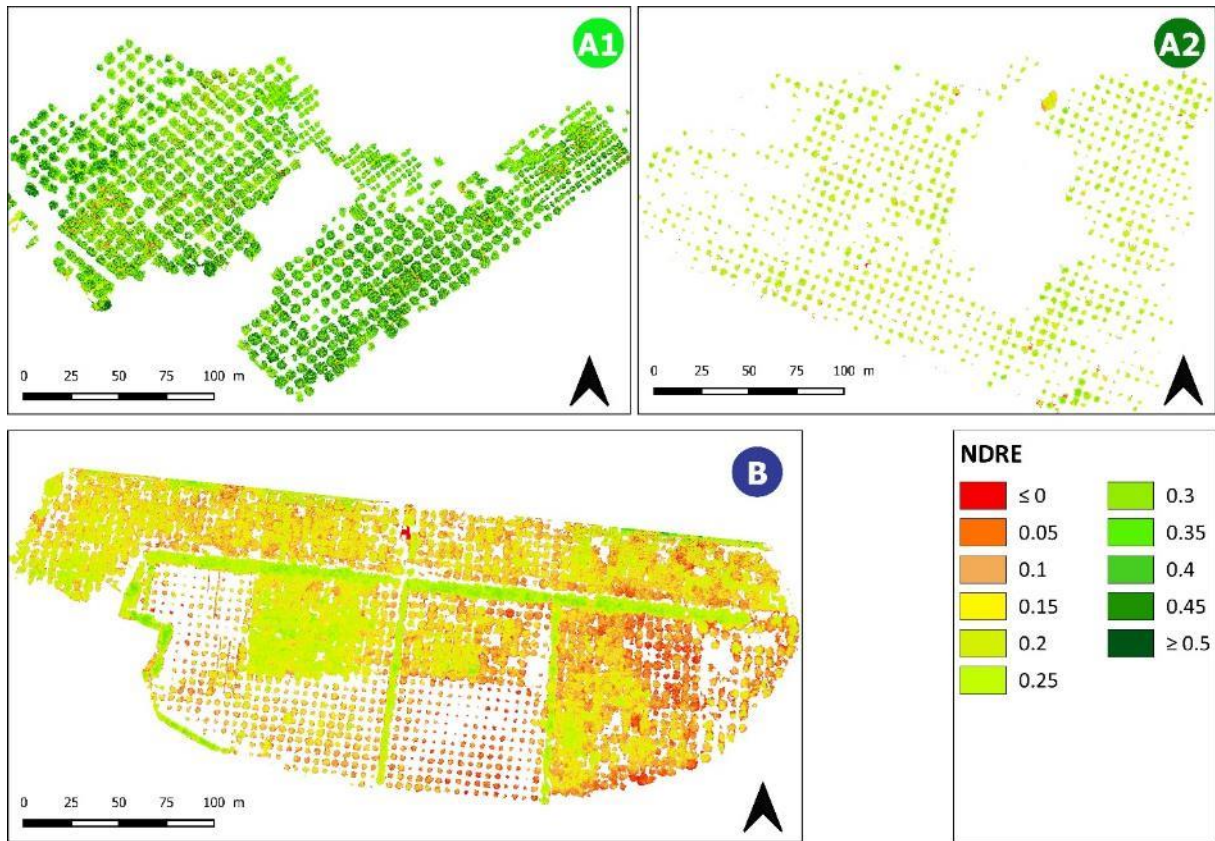
614 **Fig. 12** - Vegetative vigor maps of the three analyzed study sites [A1 (Clementine), A2 (Olive), and B (Bergamot  
615 and Olive)] based on the Normalized Difference Vegetation Index (NDVI) values.

616

617 Looking at the NDRE (Fig. 13) map, the contrast between the vegetative vigor of olive trees and bergamot  
618 trees is evident. While olive trees are characterized by NDRE values from 0.25 and up, the highest value for  
619 bergamot trees is 0.25 and can be found only in sectors 5 and 8. As also shown by the NDVI, the lowest  
620 values of NDRE are in the lower part of sector 4 and in the middle between sectors 2 and 1, which are the  
621 areas closest to the sea.

622 Besides, two aspects cannot be overlooked. The first one concerns the size of the analyzed study sites,  
623 comprised from 4.6 to 7.9 ha, and whose surface is comparable to operational conditions. The second aspect  
624 also concerns an operational issue. The time needed for the complete implementation of our proposed  
625 workflow, from the on-field data collection to the obtaining of vigor maps, can be estimated in one working  
626 day of two good skilled operators in geomatics and computer image processing. All data processing was  
627 implemented in a workstation with the following characteristics: OS MS Windows 10 Pro, CPU Intel dual  
628 Xeon E5-2687W v2, 64 GB RAM DDR3 1866 MHz, GPU NVIDIA K6000.

629



630

631

632 **Fig. 13** - Vegetative vigor maps of the three analyzed study sites [A1 (Clementine), A2 (Olive), and B (Bergamot  
633 and Olive)] based on the Normalized Difference Red Edge Vegetation Index (NDRE) values.

634

## 635 5. Conclusions

636 In the present research work, we propose a quick and reliable semi-automatic workflow implemented to  
637 process multispectral UAV imagery and aimed at the detection and extraction of olive and citrus trees'  
638 crowns in the framework of precision agriculture PA. As confirmed by Solano et al. (2019), in the GEOBIA  
639 approach, the extraction of the trees takes advantage in orchards characterized by regular planting patterns  
640 with minimal overlap between the canopies. In our work, we demonstrated that the high spatial resolution of  
641 UAV allows overcoming these limitations. Moreover, the use of a UAV platform, coupled with a  
642 multispectral camera as Tetracam  $\mu$ -MCA06 Snap, has proved to be flexible and reliable in obtaining the  
643 photogrammetric reconstruction at the farming scale. Therefore, using high-resolution contents from UAV  
644 data, more focused analyses were performed only on the cultivated areas, excluding ground and shadows, in  
645 order to obtain a reasonable reconstruction of the orchards and the description of the crop conditions.

646 On the other hand, to obtain good results, good quality of UAV field surveys is a need. As highlighted in  
647 discussing the obtained accuracy, the correct UAV flight planning has a crucial role in obtaining good results,  
648 and the same is true of measures taken in the field, such as the laying of GCP. In our case, referring to study  
649 sites A2 and B, a higher buffer beyond the orchard boundary could have improved the accuracy in extracting  
650 the trees' crowns. In this regard, we suggest providing a buffer distance of at least 20 m outside the surveyed  
651 area. In the proposed workflow, we focused our attention also in simplifying the classification step and on  
652 the speed of execution. First, visual interpretation is applied to UAV imagery to acquire prior knowledge of  
653 the imagery (Ma et al., 2015). Concerning the segmentation step, scale parameters were chosen for generating  
654 segmented objects that represent real objects (Blaschke, 2010), single canopies in our case. As far as the  
655 classification is concerned, we proposed an unsupervised approach that has the advantage not to provide a  
656 training phase, and therefore the need for the selection of training samples set for training the classifier (Ma  
657 et al., 2015). The novelty of the proposed approach relies, therefore, on its speed, replicability, and reliability  
658 demonstrated with promising results in three different datasets. Agricultural environments may be more  
659 uniform than natural ones (Csillik et al., 2018). However, the present work has, among other things, dealt  
660 with the application of the proposed approach on a case (especially in dataset B) of heterogeneous tree  
661 orchards. The heterogeneity concerns different tree plantation distances and composition, different crop  
662 management, and different tree age, height, and crown diameters, therefore, resulting in the high spatial  
663 variability of the scene.

664 Following our promising results, we think that our methodology can be used in different orchards worldwide,  
665 setting the segmentation parameters properly, and after a spectral analysis. As also demonstrated by our  
666 experience and by those we cited in this paper, the use of topographic data (DSM, CHM), helps to improve  
667 the obtained results. Indeed, in implementing our workflow, we took into account its operational application.  
668 It appears worth of interest to highlights that it requests a working day of two good skilled operators in  
669 geomatics and image processing, from the on-field data collection to the obtaining of vigor maps. In this  
670 regard, for its application in different conditions of those analyzed in the present research, the time needed  
671 for its complete implementation can be estimated in one working day of two good skilled operators in  
672 geomatics and image processing. These characteristics are in line with the need of the PA to provide  
673 information, in a short space of time, useful to guide farmers' decisions.

674

675 **Acknowledgments** This research has been funded by project PON03PE\_00090\_2, in the framework of  
676 National Operational Program (NOP) for Research and Competitiveness 2007-2013 of the Italian Ministry of  
677 Education, University and Research (MIUR) and Ministry of Economic Development (MiSE), and co-funded by  
678 the European Regional Development Fund (ERDF). The authors would like to express their great appreciation to  
679 the anonymous reviewers for their very constructive comments provided during the revision of the paper and that  
680 contribute to improving it significantly.

## 681 **6. References**

- 682 Abdulridha, J., Ehsani, R., Abd-Elrahman, A., Ampatzidis, Y., 2019. A remote sensing technique for detecting  
683 laurel wilt disease in avocado in presence of other biotic and abiotic stresses. *Comput. Electron. Agric.* 156,  
684 549–557. <https://doi.org/10.1016/j.compag.2018.12.018>
- 685 Aguilar, M.A., Aguilar, F.J., García Lorca, A., Guirado, E., Betlej, M., Cichon, P., Nemmaoui, A., Vallario, A.,  
686 Parente, C., 2016. Assessment of multiresolution segmentation for extracting greenhouses from WorldView-  
687 2 imagery. *Int. Arch. Photogramm. Remote Sens. Spat. Inf. Sci. - ISPRS Arch.* 41, 145–152.  
688 <https://doi.org/10.5194/isprsarchives-XLI-B7-145-2016>
- 689 Albetis, J., Jacquín, A., Goulard, M., Poilvé, H., Rousseau, J., Clenet, H., Dedieu, G., Duthoit, S., 2018. On the  
690 Potentiality of UAV Multispectral Imagery to Detect Flavescence dorée and Grapevine Trunk Diseases.  
691 *Remote Sens.* 11, 23. <https://doi.org/10.3390/rs11010023>
- 692 Ampatzidis, Y., Partel, V., 2019. UAV-Based High Throughput Phenotyping in Citrus Utilizing Multispectral  
693 Imaging and Artificial Intelligence. *Remote Sens.* 11, 410. <https://doi.org/10.3390/rs11040410>
- 694 Baatz, M., Schape, A., 2000. Multiresolution segmentation - An optimization approach for high quality multi-  
695 scale image segmentation, in: Strobl, J., Blaschke, T., Griesbner, G. (Eds.), *Angewandte Geographische*  
696 *Informations-Verarbeitung, XII*, Wichmann Verlag, Karlsruhe, Germany, pp. 12–23.
- 697 Barnes, E.M., Clarke, T.R., Richards, S.E., Colaizzi, P.D., Haberland, J., Kostrzewski, M., Waller, P., Choi C.,  
698 R.E., Thompson, T., Lascano, R.J., Li, H., Moran, M.S., 2000. Coincident detection of crop water stress,  
699 nitrogen status and canopy density using ground based multispectral data, in: *Proc. 5th Int. Conf. Precis*  
700 *Agric.*
- 701 Barrett, E.C., Curtis, L.F., 2013. *Introduction to Environmental Remote Sensing, Introduction to Environmental*  
702 *Remote Sensing.* <https://doi.org/10.4324/9780203761038>
- 703 Benabdelkamel, H., Di Donna, L., Mazzotti, F., Naccarato, A., Sindona, G., Tagarelli, A., Taverna, D., 2012.  
704 Authenticity of PGI “clementine of Calabria” by multielement fingerprint. *J. Agric. Food Chem.* 60, 3717–  
705 3726. <https://doi.org/10.1021/jf2050075>
- 706 Bendig, J., Yu, K., Aasen, H., Bolten, A., Bennertz, S., Broscheit, J., Gnyp, M.L., Bareth, G., 2015. Combining  
707 UAV-based plant height from crop surface models, visible, and near infrared vegetation indices for biomass  
708 monitoring in barley. *Int. J. Appl. Earth Obs. Geoinf.* 39, 79–87. <https://doi.org/10.1016/j.jag.2015.02.012>
- 709 Benincasa, P., Antognelli, S., Brunetti, L., Fabbri, C.A., Natale, A., Sartoretti, V., Modeo, G., Guiducci, M., Tei,  
710 F., Vizzari, M., 2018. Reliability of ndvi derived by high resolution satellite and uav compared to in-field  
711 methods for the evaluation of early crop n status and grain yield in Wheat. *Exp. Agric.* 54, 604–622.  
712 <https://doi.org/10.1017/S0014479717000278>
- 713 Blaschke, T., 2010. Object based image analysis for remote sensing. *ISPRS J. Photogramm. Remote Sens.* 65, 2–  
714 16. <https://doi.org/10.1016/j.isprsjprs.2009.06.004>
- 715 Blaschke, T., Hay, G.J., Kelly, M., Lang, S., Hofmann, P., Addink, E., Queiroz Feitosa, R., van der Meer, F., van  
716 der Werff, H., van Coillie, F., Tiede, D., 2014. Geographic Object-Based Image Analysis – Towards a new  
717 paradigm. *ISPRS J. Photogramm. Remote Sens.* 87, 180–191.  
718 <https://doi.org/10.1016/j.isprsjprs.2013.09.014>
- 719 Campbell, J.B., Wynne., R.H., 2011. *Introduction to Remote Sensing FIFTH EDITION, Uma ética para quantos?*  
720 <https://doi.org/10.1007/s13398-014-0173-7.2>

- 721 Candiago, S., Remondino, F., De Giglio, M., Dubbini, M., Gattelli, M., 2015. Evaluating multispectral images and  
722 vegetation indices for precision farming applications from UAV images. *Remote Sens.* 7, 4026–4047.  
723 <https://doi.org/10.3390/rs70404026>
- 724 Caruso, G., Zarco-Tejada, P.J., González-Dugo, V., Moriondo, M., Tozzini, L., Palai, G., Rallo, G., Hornero, A.,  
725 Primicerio, J., Gucci, R., 2019. High-resolution imagery acquired from an unmanned platform to estimate  
726 biophysical and geometrical parameters of olive trees under different irrigation regimes. *PLoS One* 14,  
727 e0210804. <https://doi.org/10.1371/journal.pone.0210804>
- 728 Chen, G., Weng, Q., Hay, G.J., He, Y., 2018. Geographic object-based image analysis (GEOBIA): emerging trends  
729 and future opportunities. *GIScience Remote Sens.* 55, 159–182.  
730 <https://doi.org/10.1080/15481603.2018.1426092>
- 731 Csillik, O., Cherbini, J., Johnson, R., Lyons, A., Kelly, M., 2018. Identification of Citrus Trees from Unmanned  
732 Aerial Vehicle Imagery Using Convolutional Neural Networks. *Drones* 2, 39.  
733 <https://doi.org/10.3390/drones2040039>
- 734 Da Pozzo, E., De Leo, M., Faraone, I., Milella, L., Cavallini, C., Piragine, E., Testai, L., Calderone, V., Pistelli,  
735 L., Braca, A., Martini, C., 2018. Antioxidant and antisenesescence effects of bergamot juice. *Oxid. Med. Cell.*  
736 *Longev.* 2018. <https://doi.org/10.1155/2018/9395804>
- 737 De Castro, A.I., Ehsani, R., Ploetz, R., Crane, J.H., Abdulridha, J., 2015. Optimum spectral and geometric  
738 parameters for early detection of laurel wilt disease in avocado. *Remote Sens. Environ.* 171, 33–44.  
739 <https://doi.org/10.1016/j.rse.2015.09.011>
- 740 De Castro, A.I., Peña, J.M., Torres-Sánchez, J., Jiménez-Brenes, F., López-Granados, F., 2017. Mapping *Cynodon*  
741 *dactylon* in vineyards using UAV images for site-specific weed control. *Adv. Anim. Biosci.* 8, 267–271.  
742 <https://doi.org/10.1017/s2040470017000826>
- 743 De Castro, A.I., Torres-Sánchez, J., Peña, J.M., Jiménez-Brenes, F.M., Csillik, O., López-Granados, F., 2018. An  
744 automatic random forest-OBIA algorithm for early weed mapping between and within crop rows using UAV  
745 imagery. *Remote Sens.* 10, 1–21. <https://doi.org/10.3390/rs10020285>
- 746 Di Fazio, S., Modica, G., 2018. Historic rural landscapes: Sustainable planning strategies and action criteria. *The*  
747 *Italian experience in the Global and European Context.* *Sustain.* 10. <https://doi.org/10.3390/su10113834>
- 748 Díaz-Varela, R., de la Rosa, R., León, L., Zarco-Tejada, P., 2015. High-Resolution Airborne UAV Imagery to  
749 Assess Olive Tree Crown Parameters Using 3D Photo Reconstruction: Application in Breeding Trials.  
750 *Remote Sens.* 7, 4213–4232. <https://doi.org/10.3390/rs70404213>
- 751 Drăguț, L., Csillik, O., Eisank, C., Tiede, D., 2014. Automated parameterisation for multi-scale image  
752 segmentation on multiple layers. *ISPRS J. Photogramm. Remote Sens.* 88, 119–127.  
753 <https://doi.org/10.1016/j.isprsjprs.2013.11.018>
- 754 Drăguț, L., Tiede, D., Levick, S.R., 2010. ESP: a tool to estimate scale parameter for multiresolution image  
755 segmentation of remotely sensed data. *Int. J. Geogr. Inf. Sci.* 24, 859–871.  
756 <https://doi.org/10.1080/13658810903174803>
- 757 El-naggar, A.M., 2018. Determination of optimum segmentation parameter values for extracting building from  
758 remote sensing images. *Alexandria Eng. J.* 57, 3089–3097. <https://doi.org/10.1016/j.aej.2018.10.001>
- 759 Gamon, J.A., Surfus, J.S., 1999. Assessing leaf pigment content and activity with a reflectometer. *New Phytol.*  
760 143, 105–117. <https://doi.org/10.1046/j.1469-8137.1999.00424.x>
- 761 Gitelson, A.A., Kaufman, Y.J., Merzlyak, M.N., 1996. Use of a green channel in remote sensing of global  
762 vegetation from EOS- MODIS. *Remote Sens. Environ.* 58, 289–298. [https://doi.org/10.1016/S0034-4257\(96\)00072-7](https://doi.org/10.1016/S0034-4257(96)00072-7)
- 764 Giuffrè, A.M., 2019. Bergamot (*Citrus bergamia*, Risso): The effects of cultivar and harvest date on functional  
765 properties of juice and cloudy juice. *Antioxidants* 8. <https://doi.org/10.3390/antiox8070221>
- 766 Glenn, E.P., Huete, A.R., Nagler, P.L., Nelson, S.G., 2008. Relationship between remotely-sensed vegetation

- 767 indices, canopy attributes and plant physiological processes: What vegetation indices can and cannot tell us  
768 about the landscape. *Sensors*. <https://doi.org/10.3390/s8042136>
- 769 Goutte, C., Gaussier, E., 2005. A Probabilistic Interpretation of Precision, Recall and F-Score, with Implication  
770 for Evaluation. *Lect. Notes Comput. Sci.* 3408, 345–359. [https://doi.org/10.1007/978-3-540-31865-1\\_25](https://doi.org/10.1007/978-3-540-31865-1_25)
- 771 Hay, G.J., Castilla, G., 2008. Geographic object-based image analysis (GEOBIA): A new name for a new  
772 discipline. *Lect. Notes Geoinf. Cartogr.* 75–89. [https://doi.org/10.1007/978-3-540-77058-9\\_4](https://doi.org/10.1007/978-3-540-77058-9_4)
- 773 Huete, A.R., 1988. A soil-adjusted vegetation index (SAVI). *Remote Sens. Environ.* 25, 295–309.  
774 [https://doi.org/10.1016/0034-4257\(88\)90106X](https://doi.org/10.1016/0034-4257(88)90106X)
- 775 Jin, W.F., Shen, L.H., Ren, J.H., Jin, J.M., Shen, Y.Y., Zhu, J.Q., Liang, Z.S., Yang, D.F., 2016. Research progress  
776 on bergamot essential oil and its related product development. *Chinese Tradit. Herb. Drugs*.  
777 <https://doi.org/10.7501/j.issn.0253-2670.2016.05.029>
- 778 Jones, H.G., Vaughan, R.A., 2010. *Remote Sensing of Vegetation Principles, Techniques, and Applications*.  
779 Oxford University Press, Oxford, UK.
- 780 Kaufman, Y.J., Remer, L.A., 1994. Detection of Forests Using Mid-IR Reflectance: An Application for Aerosol  
781 Studies. *IEEE Trans. Geosci. Remote Sens.* 32, 672–683. <https://doi.org/10.1109/36.297984>
- 782 Khanal, S., Fulton, J., Shearer, S., 2017. An overview of current and potential applications of thermal remote  
783 sensing in precision agriculture. *Comput. Electron. Agric.* 139, 22–32.  
784 <https://doi.org/10.1016/j.compag.2017.05.001>
- 785 Koc-San, D., Selim, S., Aslan, N., San, B.T., 2018. Automatic citrus tree extraction from UAV images and digital  
786 surface models using circular Hough transform. *Comput. Electron. Agric.* 150, 289–301.  
787 <https://doi.org/10.1016/j.compag.2018.05.001>
- 788 Laliberte, A.S., Rango, A., 2009. Texture and scale in object-based analysis of subdecimeter resolution unmanned  
789 aerial vehicle (UAV) imagery. *IEEE Trans. Geosci. Remote Sens.* 47, 1–10.  
790 <https://doi.org/10.1109/TGRS.2008.2009355>
- 791 Larson, W.E., Robert, P.C., 1991. Farming by Soil, in: *Soil Management for Sustainability*. pp. 103–112.
- 792 Li, M., Ma, L., Blaschke, T., Cheng, L., Tiede, D., 2016. A systematic comparison of different object-based  
793 classification techniques using high spatial resolution imagery in agricultural environments. *Int. J. Appl.*  
794 *Earth Obs. Geoinf.* 49, 87–98. <https://doi.org/10.1016/j.jag.2016.01.011>
- 795 Li, W., Guo, Q., Jakubowski, M.K., Kelly, M., 2012. A New Method for Segmenting Individual Trees from the  
796 Lidar Point Cloud. *Photogramm. Eng. Remote Sens.* 78, 75–84. <https://doi.org/10.14358/PERS.78.1.75>
- 797 Li, W., Niu, Z., Chen, H., Li, D., Wu, M., Zhao, W., 2016. Remote estimation of canopy height and aboveground  
798 biomass of maize using high-resolution stereo images from a low-cost unmanned aerial vehicle system. *Ecol.*  
799 *Indic.* 67, 637–648. <https://doi.org/10.1016/j.ecolind.2016.03.036>
- 800 Ma, L., Cheng, L., Li, M., Liu, Y., Ma, X., 2015. Training set size, scale, and features in Geographic Object-Based  
801 Image Analysis of very high resolution unmanned aerial vehicle imagery. *ISPRS J. Photogramm. Remote*  
802 *Sens.* 102, 14–27. <https://doi.org/10.1016/j.isprsjprs.2014.12.026>
- 803 Ma, L., Li, M., Ma, X., Cheng, L., Du, P., Liu, Y., 2017. A review of supervised object-based land-cover image  
804 classification. *ISPRS J. Photogramm. Remote Sens.* 130, 277–293.  
805 <https://doi.org/10.1016/j.isprsjprs.2017.06.001>
- 806 Maes, W.H., Steppe, K., 2019. Perspectives for Remote Sensing with Unmanned Aerial Vehicles in Precision  
807 Agriculture. *Trends Plant Sci.* 24, 152–164. <https://doi.org/10.1016/J.TPLANTS.2018.11.007>
- 808 Malambo, L., Popescu, S.C., Murray, S.C., Putman, E., Pugh, N.A., Horne, D.W., Richardson, G., Sheridan, R.,  
809 Rooney, W.L., Avant, R., Vidrine, M., McCutchen, B., Baltensperger, D., Bishop, M., 2018. Multitemporal  
810 field-based plant height estimation using 3D point clouds generated from small unmanned aerial systems  
811 high-resolution imagery. *Int. J. Appl. Earth Obs. Geoinf.* 64, 31–42.  
812 <https://doi.org/10.1016/J.JAG.2017.08.014>

- 813 Mohan, M., Silva, C., Klauberg, C., Jat, P., Catts, G., Cardil, A., Hudak, A., Dia, M., Mohan, M., Silva, C.A.,  
814 Klauberg, C., Jat, P., Catts, G., Cardil, A., Hudak, A.T., Dia, M., 2017. Individual Tree Detection from  
815 Unmanned Aerial Vehicle (UAV) Derived Canopy Height Model in an Open Canopy Mixed Conifer Forest.  
816 *Forests* 8, 340. <https://doi.org/10.3390/f8090340>
- 817 De Montis, A. De, Modica, G., Arcidiacono, C., 2017. Encyclopedia of Big Data. *Encycl. Big Data*.  
818 <https://doi.org/10.1007/978-3-319-32001-4>
- 819 Nesci, F.S., Sapone, N., 2014. BERGAMOT - A Green and Multifunctional Asset Exclusive from the Province of  
820 Reggio Calabria. *Adv. Eng. Forum* 11, 376–379. <https://doi.org/10.4028/www.scientific.net/aef.11.376>
- 821 Ok, A.O., Ozdarici-Ok, A., 2018a. 2-D delineation of individual citrus trees from UAV-based dense  
822 photogrammetric surface models. *Int. J. Digit. Earth* 11, 583–608.  
823 <https://doi.org/10.1080/17538947.2017.1337820>
- 824 Ok, A.O., Ozdarici-Ok, A., 2018b. Combining orientation symmetry and LM cues for the detection of citrus trees  
825 in orchards from a digital surface model. *IEEE Geosci. Remote Sens. Lett.* 15, 1817–1821.  
826 <https://doi.org/10.1109/LGRS.2018.2865003>
- 827 Ok, A.O., Senaras, C., Yuksel, B., 2013a. Automated Detection of Arbitrarily Shaped Buildings in Complex  
828 Environments From Monocular VHR Optical Satellite Imagery. *IEEE Trans. Geosci. Remote Sens.* 51,  
829 1701–1717. <https://doi.org/10.1109/TGRS.2012.2207123>
- 830 Ozdarici-Ok, A., 2015a. Automatic detection and delineation of citrus trees from VHR satellite imagery. *Int. J.*  
831 *Remote Sens.* 36, 4275–4296. <https://doi.org/10.1080/01431161.2015.1079663>
- 832 Pajares, G., 2015. Overview and Current Status of Remote Sensing Applications Based on Unmanned Aerial  
833 Vehicles (UAVs). *Photogramm. Eng. Remote Sens.* 81, 281–330. <https://doi.org/10.14358/PERS.81.4.281>
- 834 Panagiotidis, D., Abdollahnejad, A., Surový, P., Chiteculo, V., 2017. Determining tree height and crown diameter  
835 from high-resolution UAV imagery. *Int. J. Remote Sens.* 38, 2392–2410.  
836 <https://doi.org/10.1080/01431161.2016.1264028>
- 837 Peña, J.M., Torres-Sánchez, J., de Castro, A.I., Kelly, M., López-Granados, F., 2013. Weed Mapping in Early-  
838 Season Maize Fields Using Object-Based Analysis of Unmanned Aerial Vehicle (UAV) Images. *PLoS One*.  
839 <https://doi.org/10.1371/journal.pone.0077151>
- 840 Peña, J.M., Torres-Sánchez, J., Serrano-Pérez, A., de Castro, A.I., López-Granados, F., 2015. Quantifying efficacy  
841 and limits of unmanned aerial vehicle (UAV) technology for weed seedling detection as affected by sensor  
842 resolution. *Sensors (Switzerland)* 15, 5609–5626. <https://doi.org/10.3390/s150305609>
- 843 Peña Barragán, J.M., Kelly, M., Castro, A.I. de, López Granados, F., 2012. Object-based approach for crop row  
844 characterization in UAV images for site-specific weed management. *Queiroz-Feitosa al., Ed. 4th Int. Conf.*  
845 *Geogr. Object-Based Image Anal. (GEOBIA 2012)*, Rio Janeiro, Brazil 426–430.
- 846 Pérez-Ortiz, M., Peña, J.M., Gutiérrez, P.A., Torres-Sánchez, J., Hervás-Martínez, C., López-Granados, F., 2016.  
847 Selecting patterns and features for between- and within- crop-row weed mapping using UAV-imagery.  
848 *Expert Syst. Appl.* 47, 85–94. <https://doi.org/10.1016/j.eswa.2015.10.043>
- 849 Pérez-Ortiz, M., Peña, J.M., Gutiérrez, P.A., Torres-Sánchez, J., Hervás-Martínez, C., López-Granados, F., 2015.  
850 A semi-supervised system for weed mapping in sunflower crops using unmanned aerial vehicles and a crop  
851 row detection method. *Appl. Soft Comput.* 37, 533–544. <https://doi.org/10.1016/j.asoc.2015.08.027>
- 852 Pernice, R., Borriello, G., Ferracane, R., Borrelli, R.C., Cennamo, F., Ritieni, A., 2009. Bergamot: A source of  
853 natural antioxidants for functionalized fruit juices. *Food Chem.* 112, 545–550.  
854 <https://doi.org/10.1016/j.foodchem.2008.06.004>
- 855 Popescu, S.C., 2007. Estimating biomass of individual pine trees using airborne lidar. *Biomass and Bioenergy* 31,  
856 646–655. <https://doi.org/10.1016/j.biombioe.2007.06.022>
- 857 Prošek, J., Šimová, P., 2019. UAV for mapping shrubland vegetation: Does fusion of spectral and vertical  
858 information derived from a single sensor increase the classification accuracy? *Int. J. Appl. Earth Obs. Geoinf.*

- 859 75, 151–162. <https://doi.org/10.1016/j.jag.2018.10.009>
- 860 Romero-Trigueros, C., Nortes, P.A., Alarcón, J.J., Hunink, J.E., Parra, M., Contreras, S., Droogers, P., Nicolás,  
861 E., 2017. Effects of saline reclaimed waters and deficit irrigation on Citrus physiology assessed by UAV  
862 remote sensing. *Agric. Water Manag.* 183, 60–69. <https://doi.org/10.1016/j.agwat.2016.09.014>
- 863 Roth, L., Streit, B., 2018. Predicting cover crop biomass by lightweight UAS-based RGB and NIR photography:  
864 an applied photogrammetric approach. *Precis. Agric.* 19, 93–114. [https://doi.org/10.1007/s11119-017-9501-](https://doi.org/10.1007/s11119-017-9501-1)  
865 1
- 866 Rouse Jr., J.W., Haas, R.H., Schell, J.A., Deering, D.W., 1974. Monitoring vegetation systems in the great plains  
867 with erts, in: *NASA SP-351, 3rd ERTS-1 Symposium*. pp. 309–317.
- 868 Rutzinger, M., Rutzinger, M., Rottensteiner, F., Rottensteiner, F., Pfeifer, N., 2009. A Comparison of Evaluation  
869 Techniques for Building Extraction from Airborne Laser Scanning. *IEEE J. Sel. Top. Appl. Earth Obs.*  
870 *Remote Sens.* 2, 11–20. <https://doi.org/10.1109/JSTARS.2009.2012488>
- 871 Senthilnath, J., Kandukuri, M., Dokania, A., Ramesh, K.N., 2017. Application of UAV imaging platform for  
872 vegetation analysis based on spectral-spatial methods. *Comput. Electron. Agric.* 140, 8–24.  
873 <https://doi.org/10.1016/j.compag.2017.05.027>
- 874 Sepulcre-Cantó, G., Zarco-Tejada, P.J., Sobrino, J.A., Jiménez-Muñoz, J.C., Villalobos, F.J., 2005. Spatial  
875 variability of crop water stress in an olive grove with high-spatial thermal remote sensing imagery. *Precis.*  
876 *Agric.* 2005, ECPA 2005 267–272.
- 877 Shufelt, J.A., 1999. Performance evaluation and analysis of monocular building extraction from aerial imagery.  
878 *IEEE Trans. Pattern Anal. Mach. Intell.* 21, 311–326. <https://doi.org/10.1109/34.761262>
- 879 Sokolova, M., Japkowicz, N., Szpakowicz, S., 2006. Beyond Accuracy, F-Score and ROC: A Family of  
880 Discriminant Measures for Performance Evaluation. pp. 1015–1021. [https://doi.org/10.1007/11941439\\_114](https://doi.org/10.1007/11941439_114)
- 881 Solano, F., Di Fazio, S., Modica, G., 2019. A methodology based on GEOBIA and WorldView-3 imagery to derive  
882 vegetation indices at tree crown detail in olive orchards. *Int. J. Appl. Earth Obs. Geoinf.* 83, 101912.  
883 <https://doi.org/10.1016/j.jag.2019.101912>
- 884 Taylor, P., Silleos, N.G., 2006. Vegetation Indices : Advances Made in Biomass Estimation and Vegetation  
885 Monitoring in the Last 30 Years Vegetation Indices : Advances Made in Biomass Estimation and Vegetation  
886 Monitoring in the Last 30 Years. *Geocarto Int.* 37–41.  
887 <https://doi.org/https://doi.org/10.1080/10106040608542399>
- 888 Torres-Sánchez, J., López-Granados, F., Peña, J.M., 2015. An automatic object-based method for optimal  
889 thresholding in UAV images: Application for vegetation detection in herbaceous crops. *Comput. Electron.*  
890 *Agric.* 114, 43–52. <https://doi.org/10.1016/j.compag.2015.03.019>
- 891 Trimble Inc., 2019. eCognition ® Developer 1–266.
- 892 Trimble Inc., 2017. eCognition Developer 9.1.
- 893 Vincini, M., Frazzi, E., D’Alessio, P., 2007. Comparison of narrow-band and broad-band vegetation indices for  
894 canopy chlorophyll density estimation in sugar beet, in: *Precision Agriculture 2007 - Papers Presented at the*  
895 *6th European Conference on Precision Agriculture, ECPA 2007*. pp. 189–196.
- 896 Wang, F., Huang, J., Tang, Y., Wang, X., 2007. New Vegetation Index and Its Application in Estimating Leaf  
897 Area Index of Rice. *Rice Sci.* 14, 195–203. [https://doi.org/10.1016/s1672-6308\(07\)60027-4](https://doi.org/10.1016/s1672-6308(07)60027-4)
- 898 Wang, P., Feng, X., Zhao, S., Xiao, P., Xu, C., 2007. Comparison of object-oriented with pixel-based classification  
899 techniques on urban classification using TM and IKONOS imagery. *Geoinformatics 2007 Remote. Sensed*  
900 *Data Inf.* 6752, 67522J. <https://doi.org/10.1117/12.760759>
- 901 Wójtowicz, M., Wójtowicz, A., Piekarczyk, J., 2016. Application of remote sensing methods in agriculture.  
902 *Commun. Biometry Crop Sci.* 11, 31–50.
- 903 Xue, J., Su, B., 2017. Significant Remote Sensing Vegetation Indices: A Review of Developments and

- 904 Applications. *J. Sensors* 2017, 1–17. <https://doi.org/10.1155/2017/1353691>
- 905 Yao, H., Qin, R., 2019. Unmanned Aerial Vehicle for Remote Sensing Applications — A Review 1–22.
- 906 Zarco-Tejada, P.J., Diaz-Varela, R., Angileri, V., Loudjani, P., 2014. Tree height quantification using very high  
907 resolution imagery acquired from an unmanned aerial vehicle (UAV) and automatic 3D photo-reconstruction  
908 methods. *Eur. J. Agron.* 55, 89–99. <https://doi.org/10.1016/j.eja.2014.01.004>
- 909 Zhang, N., Wang, M., Wang, N., 2002. Precision agriculture - A worldwide overview, in: *Computers and*  
910 *Electronics in Agriculture*. pp. 113–132. [https://doi.org/10.1016/S0168-1699\(02\)00096-0](https://doi.org/10.1016/S0168-1699(02)00096-0)
- 911

## 912 **Figure captions**

913 Fig. 1. Geographic location and descriptive photos of the three study sites, A1 (Clementine), A2 (Olive) and B  
914 (Bergamot and olive) orchard.

915 Fig. 2 - Workflow of the proposed methodology for the vegetation monitoring at tree crown detail from unmanned  
916 aerial vehicles (UAVs) multispectral imagery in heterogeneous citrus and olive orchards.

917 Fig. 3. Upper side (1), the UAV Multirotor G4 Surveying-Robot (Service Drone GmbH) equipped with Tetracam  
918  $\mu$ -MCA06 snap multispectral camera; camera mounted on UAV gimbal and ready to capture images (2). Lower  
919 side (3), a graphical scheme showing how the UAV takes into account the 3D morphology of the surveyed area,  
920 guaranteeing a constant height of flight and (4) a 3D view of a flight plan.

921 Fig. 4 - Map showing the study site B with, highlighted in red, the ten parcels identified according to the irrigation  
922 scheme arranged for the bergamot orchard.

923 Fig. 5 – Study site A1. Scatter plot matrix showing all bivariate relationships between the input layer bands. For  
924 each scatterplot, implemented using the 2D kernel density estimate (KDE) with a Gaussian function, the  
925 correlation line (in red) was provided. The main diagonal reports the histograms showing the frequency distribution  
926 of pixel values while, in the upper half-matrix, Pearson's correlation (R) coefficients for all pairwise combinations  
927 of variables are reported.

928 Fig. 6 - Study site A2. Scatter plot matrix showing all bivariate relationships between the input layer bands. For  
929 each scatterplot, implemented using the 2D kernel density estimate (KDE) with a Gaussian function, the  
930 correlation line (in red) was provided. The main diagonal reports the histograms showing the frequency distribution  
931 of pixel values while, in the upper half-matrix, Pearson's correlation (R) coefficients for all pairwise combinations  
932 of variables are reported.

933 Fig. 7 - Study site B. Scatter plot matrix showing all bivariate relationships between the input layer bands. For  
934 each scatterplot, implemented using the 2D kernel density estimate (KDE) with a Gaussian function, the  
935 correlation line (in red) was provided. The main diagonal reports the histograms showing the frequency distribution  
936 of pixel values while, in the upper half-matrix, Pearson's correlation (R) coefficients for all pairwise combinations  
937 of variables are reported.

938 Fig. 8 - Land use maps of the three study sites obtained applying the implemented image object classification  
939 workflow. A1(Clementine), A2 (Olive) and B (Bergamot and Olive).

940 Fig. 9 – Maps showing a visual picture of the obtained accuracy in the analyzed three study sites [A1 (Clementine),  
941 A2 (Olive) and B (Bergamot and Olive)], using the onscreen digitized canopy boundaries as reference data.  
942 Reference crowns (Rc) are in blue, true positives (TP) are in green, false negatives (FN) in red, and false positives  
943 (FP) in yellow.

944 Fig. 10 - Average spectral profiles of reference crowns (Rc) (in blue), true positives (TP) (in green), false negatives  
945 (FN) (in red), and false positives (FP) (in yellow) in the analyzed three study sites, A1 (Clementine), A2 (Olive)  
946 and B (Bergamot and Olive).

947 Fig. 11 - Correlation matrix between the six selected vegetation indices (VIs) implemented only using the class of  
948 trees (bergamot, clementine and olive) as input data.

949 Fig. 12 - Vegetative vigour maps of the three analyzed study site [A1 (Clementine), A2 (Olive) and B (Bergamot  
950 and Olive)] based on the Soil-Adjusted Vegetation Index (SAVI) values.

951 Fig. 13 - Vegetative vigour maps of the three analyzed study site [A1 (Clementine), A2 (Olive) and B (Bergamot  
952 and Olive)] based on the Normalized Difference Red Edge Vegetation Index (NDRE) values.

953 **Table captions**

954 Tab. 1. Tetracam  $\mu$ -MCA06 snap (Global shutter) sensor characteristics bands specification (wavelength and  
955 bandwidth).

956 Tab. 2 - Flight and UAV dataset characteristics.

957 Tab. 3 - Formulation of the six vegetation indices (VIs) used in the present research.

958 Tab. 4 - Results and accuracy indicators of the trees' crowns extraction (TP, true positives; FP, false positives;  
959 FN, false negatives; r, recall; p, precision; branching factor, BF).